

# Sommerfeld Effect and Bound State Formation for Dark Matter Models with Colored Mediators with SE+BSF4DM

Mathias Becker <sup>1,2,\*</sup> Emanuele Copello <sup>3,†</sup> Julia Harz <sup>3,‡</sup> and Martin Napetschnig <sup>3,4,§</sup>

<sup>1</sup>*Dipartimento di Fisica e Astronomia, Università degli Studi di Padova, Via Marzolo 8, 35131 Padova, Italy*

<sup>2</sup>*INFN, Sezione di Padova, Via Marzolo 8, 35131 Padova, Italy*

<sup>3</sup>*PRISMA<sup>+</sup> Cluster of Excellence & Mainz Institute for Theoretical Physics, Johannes Gutenberg-Universität Mainz, 55099 Mainz, Germany*

<sup>4</sup>*Technical University of Munich, TUM School of Natural Sciences, Physics Department T70, 85748 Garching, Germany*

(Dated: January 7, 2026)

In the universal framework of simplified  $t$ -channel dark matter models, the calculation of the relic abundance can be dominated by mediator annihilation when the dark matter and mediator masses are almost degenerate. We analyze four representative models with scalar and fermionic mediators, confront them with direct detection limits and highlight the differences and common features between them. The mediator annihilations are considerably enhanced by the Sommerfeld effect and bound state formation. Albeit their effect is subdominant in the coannihilation regime, excited bound state levels are included as well. We find that Sommerfeld and bound-state effects can lead to  $\mathcal{O}(1)$  corrections to the constraints on the DM mass in the coannihilating regime, with the precise magnitude depending on the specific model realization. In addition we provide SE+BSF4DM, an intuitive and easy to use add-on to micrOMEGAs, allowing for an automated inclusion of these effects for a generic  $t$ -channel Dark Matter Model, which is publicly available on  [Github](#).

## I. INTRODUCTION

The nature of dark matter (DM) remains one of the most pressing open questions in astroparticle physics. Despite extensive efforts to constrain weakly interacting massive particles (WIMPs) experimental searches have severely cornered the parameter space of classical WIMPs in the 10- few 100 GeV mass range [1–8]. This has spurred interest in rich dark sectors [9], where DM emerges as the lightest stable particle (LSP). Not only do such scenarios allow for much higher DM masses in the multi-TeV range due to coannihilation [10–13], but they also open up the possibility that the coannihilating partners exhibit (gauge) interactions with the standard model (SM), which are prohibited for the DM candidate itself. Such a scenario has attracted a lot of attention in recent

years [14–18].

Owing to the fact that the dark sector particles are non-relativistic in the standard freeze-out paradigm, non-perturbative effects can have a sizeable impact on the effective annihilation cross section and need to be taken into account for an accurate prediction of the DM relic density in case the dark sector particles are subject to a long-range force. The *Sommerfeld effect* [19–24] can enhance or suppress the cross section depending on the long-range potential being attractive or repulsive (see Sec. III A). Radiative formation and subsequent decay of dark sector *bound states* constitute an additional annihilation channel that can even be the dominant contribution to the total cross section, especially if colored coannihilations take place due to the strong QCD coupling [25–30].

In order to constrain the available parameter space using experimental data, it is essential to minimize the number of free parameters in a given model. This leads to the concept of *minimal*, or *simplified* dark matter models, which serve as benchmarks for experimental searches [31–41].

\* [mathias.becker@unipd.it](mailto:mathias.becker@unipd.it)

† [ecopello@uni-mainz.de](mailto:ecopello@uni-mainz.de)

‡ [julia.harz@uni-mainz.de](mailto:julia.harz@uni-mainz.de)

§ [martin.napetschnig@tum.de](mailto:martin.napetschnig@tum.de)

Simplified  $t$ -channel DM models (*DMSimp*) are a widely studied class of models, in which the mediator couples directly to DM and a SM quark [42–52]. In these setups, the mediator shares the same quantum numbers as the quark it couples to, while the DM candidate is a SM singlet. This contrasts with simplified  $s$ -channel DM models (*DMSimp*) [53], where both the mediator and the DM candidate are mostly SM singlets.

In this work, we analyze four realizations of simplified  $t$ -channel dark matter models, comparing scalar and fermionic mediators coupled to either the lightest (up) or the heaviest (top) SM quarks (see Tab. I). We quantify the impact of the aforementioned non-perturbative effects - Sommerfeld enhancement and bound-state formation (BSF) - on the dark matter relic abundance and associated mass constraints, with particular emphasis on coannihilation regimes where long-range QCD effects can enhance cross sections by up to 300% [54]. We derive updated direct detection limits and show that these effects can significantly shift the allowed dark matter mass range. To enable efficient and consistent relic density calculations, we introduce **SE+BSF4DM**, an automated C++ package that incorporates Sommerfeld and bound-state effects to the DM abundance calculation of **micrOMEGAs**. While several tools exist for generic relic density computations [55–59], the

inclusion of long-range effects remains largely unautomated. So far the only software package that provided next-to-leading order corrections including the Sommerfeld effect interfaced to **micrOMEGAs** has been **DM@NLO** [12, 24, 58, 60–64], which is so far limited to the Minimal Supersymmetric Model (MSSM) only. The recent release of **BSFfast** [65] provides highly efficient tabulations of bound-state formation cross sections for extensive phenomenological scans. The **SE+BSF4DM** package eliminates the need for manual implementations for any model within, or mappable onto, the *DMSimp* class by performing a direct, automated calculation of both Sommerfeld effect and bound state formation within the **micrOMEGAs** environment, offering a complementary approach focused on integration and ease of use for this specific framework.

This paper is structured as follows: section II briefly presents the *DMSimp* class of models and revisits the basics of DM freeze-out. Section III is devoted to a concise discussion of the Sommerfeld effect and bound state formation (BSF) in non-Abelian gauge theories. We apply our code to four representative models to highlight the impact of the non-perturbative effects, present our results and direct detection limits in section IV and summarize in Sec. V. Appendix A gives further details about the color decomposition of the QCD potential. The numerical implementation and illustrative examples on how to use our code is provided in Appendix B.

TABLE I: Summary of  $t$ -channel models considered in this work.

	up-quark	top-quark
Scalar mediator	<b>S3MuR:</b> $\mathcal{L}_{\text{int}} = g_{\text{DM}} (\bar{\chi} X^\dagger u_R + \bar{u}_R X \chi)$	<b>S3MtR:</b> $\mathcal{L}_{\text{int}} = g_{\text{DM}} (\bar{\chi} X^\dagger t_R + \bar{t}_R X \chi)$
Fermionic mediator	<b>F3SuR:</b> $\mathcal{L}_{\text{int}} = g_{\text{DM}} (\bar{X} \chi u_R + \bar{u}_R \chi X)$	<b>F3StR:</b> $\mathcal{L}_{\text{int}} = g_{\text{DM}} (\bar{X} \chi t_R + \bar{t}_R \chi X)$

## II. SIMPLIFIED $t$ -CHANNEL MODELS AND DARK MATTER COSMOLOGY

In the following, we briefly review the *DM-Simp* class of simplified  $t$ -channel DM models,

for which our code is applicable [45]. In its most general form, the DM candidate in these models, denoted generically with  $\chi$ , is a SM singlet and can either be a real or complex spin-0, spin-1/2 or spin-1 field. A  $\mathbb{Z}_2$  symmetry ensures the stability of the LSP. The mediator, generi-

cally denoted by  $X$ , couples the DM candidate to either the left-handed quark doublet, right-handed down- or up-type quark field, which are denoted by  $Q, d$  and  $u$ , respectively. The mediator may either be a spin-0 or spin-1/2 particle (real or complex)<sup>1</sup>. The three quark types times the three possible mediator spins allow for nine different Yukawa couplings  $g_{\text{DM}}$  at the renormalizable level:

$$\mathcal{L}_{\text{int}} = g_{\text{DM}} \chi \tilde{X} \tilde{q} + \text{h.c.}, \quad (1)$$

where  $\tilde{q} = Q, u, d$  and  $\tilde{X} = X^\dagger, \bar{X}$  in the case of a scalar or fermionic mediator, respectively.

For definiteness, we focus on four different realizations of the aforementioned  $t$ -channel interactions with a single Yukawa coupling  $g_{\text{DM}}$  between one mediator species and one single quark flavor. However, our code is applicable to more complicated setups as well. Adopting a similar notation to Ref. [45], our models are summarized in Tab. I.

In the S3M (F3S) models, the DM candidate is a Majorana fermion (real scalar) while the mediator is a complex scalar (Dirac fermion). For both models we consider the option of couplings to the right-handed up-quark (uR) and the right-handed top-quark (tR). The coupling to down-type quark fields gives similar results [43, 47]. The impact of Sommerfeld effect and bound state formation on the relic density for one representative model coupling to left-handed quarks was shown in S3Muni for universal couplings in Ref. [47].

At the mass scale of the DM mediators, we set the couplings of the dark scalars (which we, for the moment, denote by  $\Phi$ ) to the SM Higgs to zero:  $\lambda_{|\Phi|^2 H^2}(\mu = M_\Phi) = 0$ , such that they have no impact on the relic abundance.<sup>2</sup> However, as it has been pointed out in [18], at lower scales such couplings can grow sizeable due to their Renormalization Group (RG) running. We therefore include this running in the direct detection amplitudes.

The total dark sector number density  $n_{\text{tot}}$  divided by the entropy density  $s$  defines the total DM *yield*

$\tilde{Y} = \frac{n_{\text{tot}}}{s}$ , which, in our setup, is given by:

$$\tilde{Y} = Y_\chi + (Y_X + Y_{X^\dagger}) = Y_\chi + 2 Y_X. \quad (2)$$

The Boltzmann equation describing the evolution of the yield is expressed in terms of the dimensionless variable  $x = m_{\text{DM}}/T$ , where  $m_{\text{DM}}$  is the mass of the DM candidate (i.e. the LSP  $\chi$ ) and  $T$  is the temperature of the SM thermal bath. The time evolution of  $\tilde{Y}$  is then given by [10]

$$\frac{d\tilde{Y}}{dx} = -c g_{*,\text{eff}}^{1/2} \frac{\langle \sigma_{\text{eff}} v_{\text{rel}} \rangle}{x^2} (\tilde{Y}^2 - \tilde{Y}_{\text{eq}}^2), \quad (3)$$

where  $c = \sqrt{\pi/45} M_{\text{Pl}} m_{\text{DM}}$  with  $M_{\text{Pl}}$  being the Planck mass. The factor  $g_{*,\text{eff}}^{1/2} = \frac{g_* S}{\sqrt{g_*}} \left(1 + \frac{T}{3g_* S} \frac{dg_*}{dT}\right)$  encodes the *effective* degrees of freedom of the thermal bath, where  $g_*$  and  $g_* S$  represent, respectively, the energy and entropy degrees of freedom. The equilibrium yields for the DM candidate  $\chi$  and mediator  $X$  are [67]

$$Y_\chi^{\text{eq}} \equiv \frac{n_\chi}{s} \simeq \frac{90}{(2\pi)^{7/2}} \frac{g_\chi}{g_* S} x^{3/2} e^{-x}, \quad (4)$$

$$Y_X^{\text{eq}} = Y_{X^\dagger}^{\text{eq}} \simeq \frac{90}{(2\pi)^{7/2}} \frac{g_X}{g_* S} [(1 + \delta)x]^{3/2} e^{-(1+\delta)x}, \quad (5)$$

with  $g_\chi$  and  $g_X$  being the internal degrees of freedom of  $\chi$  and  $X$ , respectively and we introduced the relative mass splitting between the mediator and DM,

$$\delta \equiv \frac{m_X - m_\chi}{m_\chi} = \frac{\Delta m}{m_\chi}. \quad (6)$$

The effective annihilation cross section is then given by [10]:

$$\langle \sigma_{\text{eff}} v_{\text{rel}} \rangle = \sum_{ij} \langle \sigma_{ij} v_{ij} \rangle \frac{Y_i^{\text{eq}} Y_j^{\text{eq}}}{\tilde{Y}^{\text{eq}} Y^{\text{eq}}}, \quad (7)$$

The validity of Eq. (7) requires: *i*) kinetic equilibrium between the dark sector and SM bath and *ii*) chemical equilibrium within the dark sector. Both conditions are satisfied when the  $t$ -channel coupling  $g_{\text{DM}}$  is sufficiently large. While condition *i*) is generally maintained through QCD interactions of the mediators,  $g_{\text{DM}}$  must still be large enough to ensure efficient momentum transfer between the mediators and the DM. Condition *ii*) imposes a stronger requirement - the conversion rate  $\Gamma^{X \rightarrow X}$  must exceed the Hubble rate, which occurs

<sup>1</sup> Vector mediators are not included in the *DMSimpt* class. Apart from few exceptions (e.g. [66]), vector fields in the fundamental representation of  $SU(3)$  are rarely studied, because vector fields usually serve as gauge bosons and not as  $t$ -channel mediators.

<sup>2</sup> We also assume quartic self interactions of  $\Phi$  to be negligible for our analysis.

at larger  $g_{\text{DM}}$  values than needed for kinetic equilibrium. When both conditions are met, the system can be described by the single Boltzmann equation, Eq. (3), and – in case of small mass differences  $\delta$  – is the so-called **coannihilation regime**, on which we focus in this work. If  $\Gamma^{X \rightarrow X}$  is comparable to the Hubble rate during mediator freeze-out,  $H(T = m_X)$ , the conversion rates have to be explicitly included in the Boltzmann equations and one can no longer define a single effective annihilation cross section as in Eq. (7). This scenario is dubbed **conversion-driven freeze-out** [68] or **coscattering** [69]. Lastly, for even lower values of  $g_{\text{DM}}$ , the DM candidate  $\chi$  is never in thermal contact with the thermal bath and the mediator  $X$  is extremely long lived, such that the majority of DM is produced due to mediator decays before or after its thermal freeze-out. This is called the **freeze-in** [70] or **super-WIMP** scenario [71–73], respectively. The effect of Sommerfeld enhancement and bound state formation in the coannihilation regime has been assessed in Refs. [26–30, 47, 54, 74, 75]. In the coscattering and super-WIMP regime, Refs. [76–78] have also included the effects of excited bound states.

### III. LONG-RANGE EFFECTS IN SIMPLIFIED $t$ -CHANNEL MODELS

In the following, we summarize the key expressions for the Sommerfeld effect and bound state formation. Before, some general definitions for the non-relativistic central-force problem for two colored particles are given, which are used throughout this paper.

The annihilating mediators are generically denoted with  $X_1$  and  $X_2$ , have masses  $m_{X_1}$  and  $m_{X_2}$  and are in the representations  $\mathbf{R}_1$  and  $\mathbf{R}_2$  of  $SU(3)_c$ , respectively. In the simplified  $t$ -channel DM models, the representations are restricted to be the fundamental or the anti-fundamental representation:  $\mathbf{R}_i = \mathbf{3}, \bar{\mathbf{3}}, i = 1, 2$ . The reduced mass of the two-body system is given by  $\mu = \frac{m_{X_1} m_{X_2}}{m_{X_1} + m_{X_2}}$  and the possible color representations of the initial and final states are obtained by considering the decompositions into irreducible representations:

$$\mathbf{3} \otimes \bar{\mathbf{3}} = \mathbf{1} \oplus \mathbf{8} \quad (8)$$

$$\mathbf{3} \otimes \mathbf{3} = \bar{\mathbf{3}} \oplus \mathbf{6} \quad (9)$$

$$\bar{\mathbf{3}} \otimes \bar{\mathbf{3}} = \mathbf{3} \oplus \bar{\mathbf{6}}. \quad (10)$$

The strong gauge coupling  $\alpha_s$  depends on the energy scale  $Q$  and the Coulombic potential depends on the irreducible representation of the final or initial state:

$$V_{[\hat{\mathbf{R}}]}(r) = -\frac{\alpha_g^{[\hat{\mathbf{R}}]}(Q)}{r}, \quad (11)$$

where we introduced the effective coupling constant  $\alpha_g^{[\hat{\mathbf{R}}]}(Q)$  given by

$$\alpha_g^{[\hat{\mathbf{R}}]}(Q) = \alpha_s(Q) \times \frac{1}{2} [C_2(\mathbf{R}_1) + C_2(\mathbf{R}_2) - C_2(\hat{\mathbf{R}})] \quad (12)$$

$$\equiv \alpha_s(Q) \times k_{[\hat{\mathbf{R}}]}, \quad (13)$$

where  $C_2(\mathbf{R})$  are the quadratic Casimirs.

Depending on the sign of  $k_{[\hat{\mathbf{R}}]}$ , the potential is either attractive or repulsive

$$V(r)_{\mathbf{3} \otimes \bar{\mathbf{3}}} = \begin{cases} -\frac{4}{3} \frac{\alpha_s}{r} & [\mathbf{1}] \\ +\frac{1}{6} \frac{\alpha_s}{r} & [\mathbf{8}] \end{cases}, \quad (14)$$

$$V(r)_{\mathbf{3} \otimes \mathbf{3}} = \begin{cases} -\frac{2}{3} \frac{\alpha_s}{r} & [\bar{\mathbf{3}}] \\ +\frac{1}{3} \frac{\alpha_s}{r} & [\mathbf{6}] \end{cases}. \quad (15)$$

The combination of  $\bar{\mathbf{3}} \otimes \bar{\mathbf{3}}$  results in the same potential as  $\mathbf{3} \otimes \mathbf{3}$  since  $C_2(\mathbf{R}) = C_2(\bar{\mathbf{R}})$ . The typical momentum scale for scattering states is given by  $k = \mu v_{\text{rel}}$ , leading to an energy  $E_{\mathbf{k}} = \frac{\mu}{2} v_{\text{rel}}^2$  of the scattering state.

The potentials introduced above modify annihilation processes through the Sommerfeld effect and, if attractive, allow for the formation of bound states. Both effects are reviewed in the following.

#### A. Color decomposition and Sommerfeld effect

The resummed exchange of gluons between the colored particles prior to annihilation can significantly modify the cross section, an effect known as the Sommerfeld effect [19–24]. At low relative velocities, multiple gluon exchanges effectively distort the wavefunction of the incoming two-particle system. This distortion either enhances or suppresses the annihilation probability compared to the perturbative calculation, depending on whether the QCD potential is attractive or repulsive in a given

color configuration. The initial two-particle state exists in a superposition of the irreducible color representations obtained from the decompositions in Eqs. (8)-(10). Each such representation evolves independently under its own distinct Coulomb-like potential, given by Eq. (14). Consequently, the non-perturbative correction differs for each color configuration. Moreover, the short-distance annihilation process has contributions from different partial waves, characterized by orbital angular momentum  $\ell$  and spin  $s$ . The full effect is therefore captured by correcting each partial wave in each color configuration with a specific Sommerfeld factor  $S_\ell^{[\mathbf{R}]}(\zeta)$ , which depends on the effective coupling strength in that representation and the relative velocity. Thus, the total cross section is obtained by summing the perturbative partial-wave cross sections  $\sigma_{\ell s}$ , each multiplied by its corresponding color projection coefficient  $c_{\ell s}^{[\mathbf{R}]}$  and its corresponding Sommerfeld factor  $S_\ell^{[\mathbf{R}]}(\zeta)$ . The parameter  $\zeta = \frac{\alpha_g^{[\mathbf{R}]}}{v_{\text{rel}}}$  quantifies the relative strength of the attractive or repulsive potential compared to the kinetic energy of the scattering state. The full Sommerfeld corrected cross section, decomposed into partial waves, reads [79, 80]

$$\sigma_{\text{SE}} = \sum_{\ell, s} \sum_{[\mathbf{R}]} c_{\ell s}^{[\mathbf{R}]} S_\ell^{[\mathbf{R}]}(\zeta) \sigma_{\ell s}, \quad (16)$$

where  $\sum_{[\mathbf{R}]} c_{\ell s}^{[\mathbf{R}]} = 1$  for all  $(\ell, s)$  contributions to the total perturbative cross section  $\sigma_{\text{pert.}} = \sum_{\ell, s} \sigma_{\ell s}$ . The second sum in Eq. (16) sums over all irreducible representations in the initial state of the process predicted by the color decomposition. The Sommerfeld factor for the  $\ell$ -th partial wave in Eq. (16) is given by

$$S_\ell^{[\mathbf{R}]} = S_\ell \left( k_{[\mathbf{R}]} \frac{\alpha_s}{v_{\text{rel}}} \right). \quad (17)$$

When employing Eq. (17) for simplified  $t$ -channel models, the four types of Sommerfeld factors needed are:

$$S_{0, [1]} = S_0 \left( \frac{4\alpha_s}{3v_{\text{rel}}} \right), \quad S_{0, [8]} = S_0 \left( \frac{-\alpha_s}{6v_{\text{rel}}} \right), \quad (18)$$

$$S_{0, [\bar{3}]} = S_0 \left( \frac{2\alpha_s}{3v_{\text{rel}}} \right), \quad S_{0, [6]} = S_0 \left( \frac{-\alpha_s}{3v_{\text{rel}}} \right). \quad (19)$$

In case of a Coulomb potential, the function  $S_0(\zeta_s)$  is given by [19, 20]

$$S_0(\zeta_s) = \frac{2\pi\zeta_s}{1 - e^{-2\pi\zeta_s}}, \quad (20)$$

where  $\zeta_s = \alpha_{g, [\mathbf{R}]} / v_{\text{rel}} = k_{[\mathbf{R}]} \alpha_s / v_{\text{rel}}$ . Depending on the sign of  $k_{[\mathbf{R}]}$ , the Sommerfeld effect results in either a significant enhancement ( $S_{0, [1]}$  and  $S_{0, [\bar{3}]}$ ) or suppression ( $S_{0, [8]}$  and  $S_{0, [6]}$ ) of the perturbative cross-section, provided that  $v_{\text{rel}} \lesssim \alpha_{g, [\mathbf{R}]}$ . Processes which are dominated by higher powers of  $v_{\text{rel}}$  require the Sommerfeld factor for higher partial waves, which is given by [79–81]

$$S_\ell^{[\mathbf{R}]}(\zeta) = S_0^{[\mathbf{R}]}(\zeta) \prod_{k=1}^{\ell} \left( 1 + \frac{\zeta^2}{k^2} \right). \quad (21)$$

It has to be emphasized that the expansion of  $\sigma v_{\text{rel}}$  in powers of  $v_{\text{rel}}$  *does not* correspond to an expansion in partial waves  $\ell$ . The leading order contributions to  $\sigma_{\ell s} v_{\text{rel}}$  start with powers of the momentum squared  $p^{2\ell}$ , but may contain contributions with powers  $p^{2\ell'}$  with  $\ell' > \ell$  as well. For example, the cross section to order  $v_{\text{rel}}^4$  can be decomposed as follows

$$\sigma v_{\text{rel}} = \underbrace{(a + b v_{\text{rel}}^2 + \dots)}_{\text{s-wave}} + \underbrace{(c v_{\text{rel}}^2 + \dots)}_{\text{p-wave}} + \mathcal{O}(v_{\text{rel}}^4). \quad (22)$$

From Eq. (22) it should be clear that a naive expansion in  $v_{\text{rel}}$  mixes contributions from different partial waves. In `micrOMEGAs`, the cross section for numerical values of  $v_{\text{rel}}$  as a function  $\sigma v_{\text{rel}}(v_{\text{rel}})$  is accessible. This can be exploited to numerically decompose the cross section as  $\sigma v_{\text{rel}} \approx a + (b+c)v_{\text{rel}}^2 + \dots$ . Since it is not numerically possible to disentangle the  $s$ - and  $p$ -wave contributions in the  $v_{\text{rel}}^2$  term, we take the pragmatic approach of employing the Sommerfeld effect only for the leading order  $v_{\text{rel}}^0$  of the  $s$ -wave contribution, which we identify as the coefficient  $a$  in the velocity expansion; this procedure introduces an error of order  $v_{\text{rel}}^2$ . The precise implementation of the Sommerfeld effect for the colored annihilation channels considered in this work is detailed in Appendix A, see Eqs. (A4)–(A8).

## B. Bound-state formation, transitions, ionizations and decays

If the potential between the particles is attractive,  $X_1$  and  $X_2$  can form hydrogen-like bound states  $\mathcal{B}(X_1 X_2)$  upon radiation of a gluon:

$$(X_1 + X_2)_{[\mathbf{R}]} \rightarrow \mathcal{B}(X_1 X_2)_{[\mathbf{R}_B]} + g_{[\mathbf{8}]}. \quad (23)$$

This process, which we refer to as bound state formation (BSF) in the following, is depicted in Fig. 1.

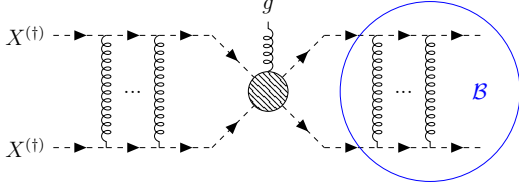


FIG. 1: Diagrammatic illustration of radiative bound state formation. The labels  $X^{(\dagger)}$  for the incoming legs indicate  $X^\dagger - X^\dagger$ ,  $X^\dagger - X$  and  $X - X$  BSF. From Ref. [47].

We focus on mediators with equal masses, for which it has been shown [47] that the rate for particle-particle BSF is strongly suppressed. While we take into account the Sommerfeld effect for all color configurations as listed in Eqs. (14) and (15), we consider therefore only  $\mathbf{3} \otimes \bar{\mathbf{3}}$  bound states and set  $\mathbf{\hat{R}} = \mathbf{8}$ ,  $\mathbf{R}_B = \mathbf{1}$  in Eq. (23).

The non-relativistic bound state  $B$  is characterized by its quantum numbers  $\{n, l, m, s\}$ , where  $n$  denotes the principal quantum number,  $l$  the orbital angular momentum,  $m$  its projection along a chosen axis, and  $s$  the total spin of the constituents. The typical momentum in a bound state with quantum number  $n$  is given by the *Bohr momentum*  $p_B = \mu \frac{\alpha_B}{n}$ , where  $\alpha_B$  is determined by solving

$$\alpha_B = \alpha_s \left( Q = \mu \frac{\alpha_B}{n} \right) \quad (24)$$

self-consistently. From the Bohr momentum, the respective binding energy can be obtained:

$$E_B = -\frac{p_B^2}{2\mu} = -\frac{1}{2}\mu \left( \frac{\alpha_B}{n} \right)^2. \quad (25)$$

Neglecting the kinetic energy of the bound states, momentum conservation fixes the energy  $\omega$  of the radiated gluon:

$$\omega \simeq E_{\mathbf{k}} - E_B = \frac{\mu}{2} \left[ v_{\text{rel}}^2 + \frac{\alpha_B^2}{n^2} \right]. \quad (26)$$

The bound state formation process is denoted by the blob in Fig. 1 and the gluon radiation is mediated by the coupling  $\alpha_{\text{BSF}} = \alpha_s(Q = \omega)$ .

The thermal average of the BSF cross section is defined as

$$\langle \sigma_{\text{BSF},i} v_{\text{rel}} \rangle = \left( \frac{\mu}{2\pi T} \right)^{3/2} \int d^3 v_{\text{rel}} \times \exp(-\mu v_{\text{rel}}^2 / 2T) [1 + f_g(\omega)] \sigma_{\text{BSF},i} v_{\text{rel}}, \quad (27)$$

with  $\omega$  given in Eq. (26) and  $f_g(\omega) = (\exp(\omega/T) - 1)^{-1}$  is the gluon distribution function. The BSF cross section itself is given by [82]

$$\sigma_{\text{BSF},i=\{n,l\}} v_{\text{rel}} = \frac{4\omega^3}{3N_c^2} \alpha_g^{[1]}(\mu v_{\text{rel}}) \times (2\ell + 1) \left| \langle \psi_{nl}^{[1]} | \mathbf{r} | \psi_{\mathbf{p}_{\text{rel}}}^{[\mathbf{8}]} \rangle \right|^2. \quad (28)$$

Here,  $\psi_{nl}^{[1]}$  denotes the non-relativistic bound-state wavefunction with principal quantum number  $n$  and orbital angular momentum  $l$ , while  $\psi_{\mathbf{p}_{\text{rel}}}^{[\mathbf{8}]}$  is the corresponding scattering-state wavefunction in the color-octet channel with relative momentum  $\mathbf{p}_{\text{rel}}$ . In a similar manner, transition rates between bound state levels can be calculated. As all these states are color singlets, the gauge boson mediating the transition cannot be a gluon. However, photon mediated transitions are allowed in our class of models. The transition rate from a higher ( $nl$ ) to a lower lying state ( $n'l'$ ) is given by [83]

$$\Gamma_{\text{trans}}^{nl \rightarrow n'l'} = \frac{4}{3} \alpha_{\text{QED}} Q_X^2 \omega_{nn'}^3 \times (2\ell + 1) |\langle \psi_{nl} | \mathbf{r} | \psi_{n'l'} \rangle|^2, \quad (29)$$

where  $\omega_{nn'} > 0$  is the difference in binding energy between the two levels ( $E_n > E_{n'}$ ), and  $\psi_{nl}$  and  $\psi_{n'l'}$  are bound state wave functions. The rate for the inverse process can be obtained via detailed balance:

$$\Gamma_{\text{trans}}^{n'l' \rightarrow nl} = \Gamma_{\text{trans}}^{nl \rightarrow n'l'} \frac{Y_{B_{nl}}^{\text{eq}}}{Y_{B_{n'l'}}^{\text{eq}}}. \quad (30)$$

Expressions for the squared matrix elements appearing in Eqs. (28) and (29) can be found in Refs. [77, 78, 84].

Bound states can be ionized by the thermal gluon plasma. The corresponding rate is given by

$$\langle \Gamma_{\text{ion}}^i \rangle = g_g \int_{\omega_{\text{min}}}^{\infty} d\omega \frac{\omega^2}{2\pi^2} f_g(\omega) \sigma_{\text{ion}}^i, \quad (31a)$$

$$\text{with } \sigma_{\text{ion}}^i = \frac{g_X^2}{g_g g_{B,i}} \left( \frac{\mu^2 v_{\text{rel}}^2}{\omega^2} \right) \sigma_{\text{BSF},i}. \quad (31b)$$

Here,  $g_X$ ,  $g_g = 8$  and  $g_{B,i}$  are the internal degrees of freedom of the mediator triplets, the gluons and the bound states  $i$ , respectively.

The decay rate  $\Gamma_{\text{dec},[\mathbf{R}]}^n$  of a  $\ell = 0$  bound state in a given representation  $\mathbf{R}$  into gluons is computed by taking the  $s$ -wave perturbative annihilation cross-section times relative velocity of the corresponding

scattering states and multiplying it with the bound state wavefunction evaluated at the origin

$$\Gamma_{\text{dec},[\mathbf{R}]}^{n\ell} = (\sigma_{\text{ann},[\mathbf{R}]}^{s\text{-wave}} v_{\text{rel}}) |\psi_{n00}^{[\mathbf{R}]}(0)|^2. \quad (32)$$

Considering the color-singlet ground state decaying into a pair of gluons, one obtains [54, 76]

$$\Gamma_{\text{dec},[1]}^n = \frac{\mu}{4n^3} C_F (\alpha_s^{\text{ann}})^2 (\alpha_{s,[1]}^B)^3, \quad (33)$$

where  $|\psi_{n00}^{[1]}(0)|^2 = \mu^3 \frac{(\alpha_{s,[1]}^B)^3}{\pi n^3}$  has been used. The decay rate for  $\ell \neq 0$  is strongly suppressed and taken to be zero.

### C. Including (excited) bound states in the Boltzmann equations

While simplified  $t$ -channel DM models feature gauge-singlet DM candidates, the color-charged mediators can undergo BSF and their annihilation are modified by the Sommerfeld effect. Thus, both the Sommerfeld effect and BSF affect can contribute efficiently to the effective annihilation cross section of DM via coannihilations. The treatment of mediator coannihilations via an effective Boltzmann equation for the dark sector is well established [10]. To incorporate BSF effects, we treat each bound state  $\mathcal{B}_i$  as an independent dynamical component having its own Boltzmann equation, analogous to the DM and mediator species. Each  $\mathcal{B}_i$  has  $g_{\mathcal{B}_i} = (2s+1)(2\ell+1)$  configurations with equal energy (degeneracy).

This gives a set of coupled Boltzmann equations between the DM candidate  $\chi$ , the mediators  $X$  and

the bound states  $\mathcal{B}_i$  [76, 85]:

$$\begin{aligned} \frac{dY_X}{dx} &= \left( \frac{dY_X}{dx} \right)_{\text{ann}} \\ &- \frac{c g_{*,\text{eff}}^{1/2}}{x^2} \left[ \sum_i \langle \sigma_{\text{BSF},i} v_{\text{rel}} \rangle \left( Y_X^2 - Y_X^{\text{eq}2} \frac{Y_{\mathcal{B}_i}}{Y_{\mathcal{B}_i}^{\text{eq}2}} \right) \right]. \end{aligned} \quad (34)$$

$$\begin{aligned} \frac{dY_{\mathcal{B}_i}}{dx} &= - \frac{c g_{*,\text{eff}}^{1/2}}{x^2} \left[ \langle \Gamma_{\text{ion}}^i \rangle \left( Y_{\mathcal{B}_i} - Y_{\mathcal{B}_i}^{\text{eq}} \frac{Y_X^2}{Y_X^{\text{eq}2}} \right) \right. \\ &+ \langle \Gamma_{\text{dec}}^i \rangle (Y_{\mathcal{B}_i} - Y_{\mathcal{B}_i}^{\text{eq}}) \\ &\left. - \sum_{j \neq i} \langle \Gamma_{\text{trans}}^{j \rightarrow i} \rangle \left( Y_{\mathcal{B}_j} - Y_{\mathcal{B}_j}^{\text{eq}} \frac{Y_{\mathcal{B}_j}}{Y_{\mathcal{B}_j}^{\text{eq}2}} \right) \right]. \end{aligned} \quad (35)$$

The equilibrium yield for the bound state species  $i$  is defined as

$$Y_{\mathcal{B}_i}^{\text{eq}} = \frac{n_{\mathcal{B}_i}^{\text{eq}}}{s} \simeq \frac{90}{(2\pi)^{7/2}} \frac{g_{\mathcal{B}_i}}{g_{*S}} \left( \frac{m_{\mathcal{B}_i}}{T} \right)^{3/2} e^{-\frac{m_{\mathcal{B}_i}}{T}}, \quad (36)$$

where  $m_{\mathcal{B}_i} = m_{X_1} + m_{X_2} - E_{\mathcal{B}_i}$  is the mass of the bound state and  $\langle \Gamma_{\text{ion}} \rangle$ ,  $\langle \Gamma_{\text{dec}} \rangle$  and  $\langle \Gamma_{\text{trans}} \rangle$  are the ionization, decay and transition rates, respectively, and are given in Sec. III B.

Since at least one of the averaged rates on the right-hand-side of the Boltzmann equation is much larger than the Hubble rate  $H$  [85], the bound state yields quickly adjust to a steady solution  $\frac{dY_{\mathcal{B}_i}}{dx} = 0$ , which turns the bound state Boltzmann equations into algebraic equations. The same applies to a single bound state, as it was first shown in Ref. [26].

All bound state effects including arbitrary many excited states can be effectively incorporated into the evolution equation for  $X$  (see Eq. (34)) in the following form [76, 85]

$$\frac{Y_{\mathcal{B}_i}}{Y_{\mathcal{B}_i}^{\text{eq}}} = 1 + \sum_j (M^{-1})_{ij} \frac{\langle \Gamma_{\text{ion}}^j \rangle}{\langle \Gamma^j \rangle} \left( \frac{Y_X^2}{Y_X^{\text{eq}2}} - 1 \right), \quad (37)$$

$$\langle \Gamma^i \rangle = \langle \Gamma_{\text{ion}}^i \rangle + \langle \Gamma_{\text{dec}}^i \rangle + \sum_{j \neq i} \langle \Gamma_{\text{trans}}^{i \rightarrow j} \rangle, \quad (38)$$

$$M_{ij} \equiv \delta_{ij} - \frac{\langle \Gamma_{\text{trans}}^{i \rightarrow j} \rangle}{\langle \Gamma^i \rangle}. \quad (39)$$

The indices  $i, j$  run over all labels of bound state quantum numbers  $(n, l, m, s)$ . With these manipulations, one obtains the following effective thermally averaged annihilation cross section for the mediators [76, 85]

$$\langle \sigma_{XX} v_{\text{rel}} \rangle_{\text{eff}} = \langle \mathcal{S}(\sigma_{XX} v_{\text{rel}}) \rangle_{\text{ann}} + \sum_i \langle \sigma_{\text{BSF},i} v_{\text{rel}} \rangle \left( 1 - \sum_j (M^{-1})_{ij} \frac{\langle \Gamma_{\text{ion}}^j \rangle}{\langle \Gamma_j \rangle} \right) \quad (40)$$

The first term in Eq. (40) contains the annihilation cross section of the mediator  $X$ , where the Sommerfeld enhancement/suppression is indicated with  $\mathcal{S}(\dots)$ . The second term captures the contribution of the bound states with the short-hand label  $i = (n, \ell, m, s)$ . Eq. (40) forms the backbone of our `micrOMEGAS` package. Limiting cases allow for simpler expressions for the effective BSF cross section in Eq. (40). These are:

- **No transition limit:**

$\langle \Gamma_{\text{dec}}^i \rangle, \langle \Gamma_{\text{ion}}^i \rangle \gg \langle \Gamma_{\text{trans}}^{i \rightarrow j} \rangle \forall i, j$ . In this limit, the matrix  $M$  in Eq. (39) becomes the trivial identity matrix. One obtains a weighted sum of bound state contributions with weight factors analogous to the ones used for the ground state [47, 54, 86, 87]

$$\langle \sigma_{\text{BSF}} v_{\text{rel}} \rangle_{\text{eff}} = \sum_i \langle \sigma_{\text{BSF},i} v_{\text{rel}} \rangle w_i \quad (41)$$

$$w_i = \frac{\langle \Gamma_{\text{dec}}^i \rangle}{\langle \Gamma_{\text{dec}}^i \rangle + \langle \Gamma_{\text{ion}}^i \rangle}. \quad (42)$$

- **Efficient transition limit:**

$\langle \Gamma_{\text{trans}}^{i \rightarrow j} \rangle \gg \langle \Gamma_{\text{ion}}^i \rangle, \langle \Gamma_{\text{dec}}^i \rangle \forall i, j$ . In this regime, transitions are so efficient that *all* bound state levels (including those with zero decay rate at leading order in  $\alpha_s$ ) contribute to the annihilation cross section. In this limit, the effective BSF cross section does not depend explicitly on the transition rates  $\langle \Gamma_{\text{trans}}^{i \rightarrow j} \rangle$ . Instead, *effective decay and ionization rates* enter in the effective bound state contribution to  $\langle \sigma_{\text{BSF}} v_{\text{rel}} \rangle_{\text{eff}}$ .

$$\langle \sigma_{\text{BSF}} v_{\text{rel}} \rangle_{\text{eff}} = \sum_i \langle \sigma_{\text{BSF},i} v_{\text{rel}} \rangle w, \quad (43)$$

$$w = \frac{\Gamma_{\text{dec}}^{\text{eff}}}{\Gamma_{\text{dec}}^{\text{eff}} + \Gamma_{\text{ion}}^{\text{eff}}}, \quad (44)$$

$$\Gamma_{\text{ion/dec}}^{\text{eff}} \equiv \frac{\sum_i \langle \Gamma_{\text{ion/dec}}^i \rangle Y_{\mathcal{B}_i}^{\text{eq}}}{\sum_j Y_{\mathcal{B}_j}^{\text{eq}}}. \quad (45)$$

In the efficient transition limit the bound

states are in chemical equilibrium among themselves.

- **Ionization equilibrium:**

$\langle \Gamma_{\text{ion}}^i \rangle \gg \langle \Gamma_{\text{dec}}^i \rangle, \langle \Gamma_{\text{trans}}^{i \rightarrow j} \rangle \forall i, j$ . This hierarchy of rates applies to high temperatures/early times, when ionization and recombination processes are in equilibrium. The effective BSF cross section is then given by:

$$\langle \sigma_{\text{BSF}} v_{\text{rel}} \rangle_{\text{eff}} = \frac{1}{g_{X_1} g_{X_2}} \times \left( \frac{2\pi}{T\mu} \right)^{3/2} \sum_i g_{\mathcal{B}_i} e^{E_{\mathcal{B}_i}/T} \Gamma_{\text{dec}}^i \quad (46)$$

This limit is rarely of practical interest, as the hierarchy  $\langle \Gamma_{\text{ion}}^i \rangle \gg \langle \Gamma_{\text{dec}}^i \rangle$  does not hold any more at low temperatures.

The user may choose between one of these three limiting scenarios with the `bsf_scenario=1,2,3` option, while the default is the full solution to Eq. (40) (`bsf_scenario=4`).

## IV. RESULTS AND DISCUSSION

### A. Impact of long-range effects on the relic density

We run parameter scans of the four  $t$ -channel models presented in Sec. II for values of  $m_{\text{DM}} \in [200, 10^4] \text{ GeV}$ ,  $\delta \in [10^{-4}, 10]$  and  $g_{\text{DM}} \in [10^{-4}, \sqrt{4\pi}]$ . For this range of  $g_{\text{DM}}$ , the dark sector is in chemical equilibrium. Moreover, colored gauge interactions ensure that the mediators  $X$  are in kinetic equilibrium with the SM. This choice of parameter space is motivated by requiring dark matter to annihilate in the non-relativistic regime, which enhances the impact of long-range effects. To ensure this, we focus on dark-matter masses above 200 GeV, so that annihilations always proceed into lighter SM states (including top quarks).

We restrict our analysis to the parameter space where the assumptions of freeze-out and coannihilation remain valid, and where perturbative unitarity is maintained. In addition, in all of our scans we ensure that  $\Delta m > 1 \text{ GeV}$ , as otherwise post-confinement annihilations of the mediators are shown to have a drastic impact on the relic density [88], because annihilations of confined hadrons with geometric cross sections boost the annihilation cross section. Moreover, we also demand that  $E_{B_s} \gtrsim \Lambda_{\text{QCD}}$ , to ensure that  $\alpha_s$  is only evaluated in its perturbative regime when determining bound-state formation cross section [84]. To emphasize the impact of long-range effects, we compare the regions of parameter space in the

$(\Delta m - m_{\text{DM}})$ -plane predicting the correct relic abundance with four different setups: *i*) The conventional perturbative calculation, *ii*) including the Sommerfeld effect, *iii*) adding bound state formation of the  $n = 1$  state and, finally, *iv*) the full tower of excited states up to  $n = 6$  according to Eq. (40). We find that the effect of excited states with  $n > 6$  changes the relic density less than 1% in the parameter space we consider. This is because excited states give a significant contribution at high values of  $x$ , which are suppressed by the exponential factor  $e^{-2\delta x}$  in the effective coannihilation cross section Eq. (7). Our comparison for the four  $t$ -channel models considered in this work is illustrated in Fig. 2.

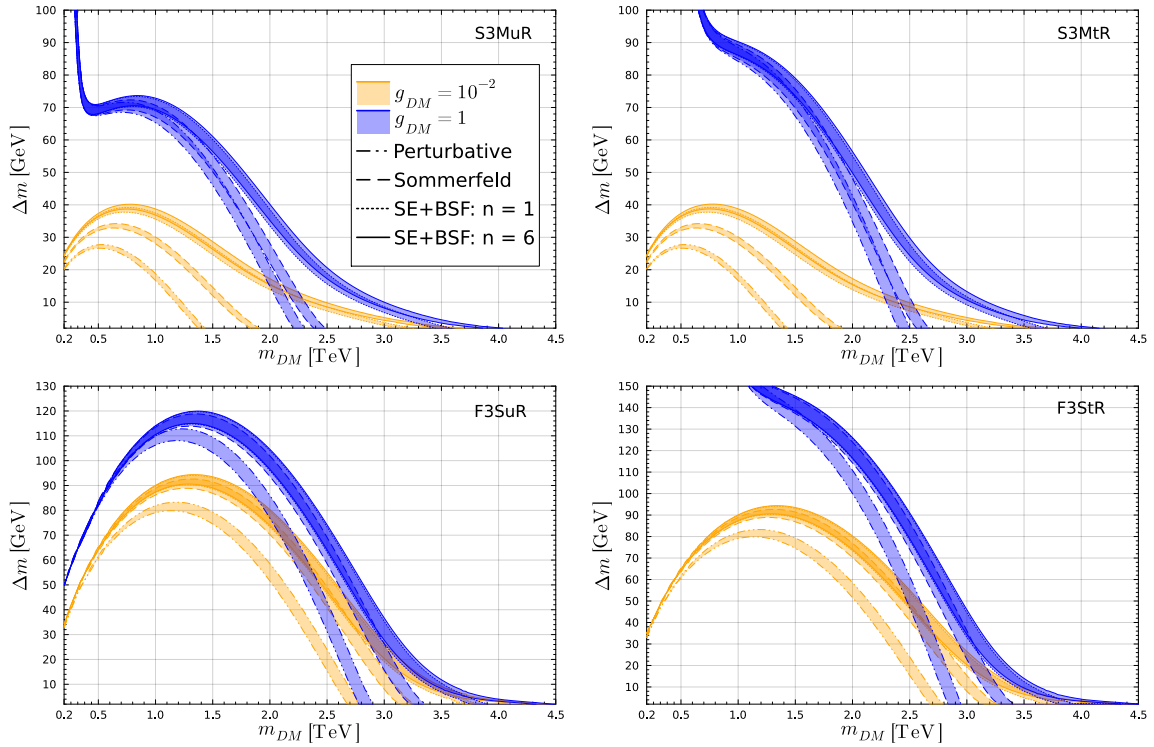


FIG. 2: Mass splitting  $\Delta m$  vs. DM mass  $m_{\text{DM}}$  for the four models considered. Blue (yellow) bands correspond to a  $5\sigma$  uncertainty of  $\Omega h^2$  [89] for  $g_{\text{DM}} = 1$  ( $10^{-2}$ ). Dash-dotted bands correspond to the conventional perturbative calculation, dashed bands include the Sommerfeld effect. Bound state formation for the ground state ( $n = 1$ ) is indicated by the dotted lines, which in most of parameter space overlay with the solid bands for  $n = 6$ .

We observe that long-range effects have a larger impact for lower  $g_{\text{DM}}$ , as in this case colored anni-

hilations of the mediators dominate. Bound state formation has its biggest impact for low mass splittings, where it is not exponentially suppressed by the coannihilation weight. Since the cross sections for excited states peak at higher values of  $x = m_{DM}/T$  than the ground state, the effect of excited states is only visible for large DM masses (see the difference between the solid and the dotted curves in Fig. 2) and hence expected to be of minor importance in the coannihilation regime (see also Ref. [76]).

The dependence on  $g_{DM}$  differs between fermionic and scalar mediators due to their distinct annihilation properties. The curves in Fig. 2 reflect the following features:

- Perturbative annihilations: F3S models naturally achieve larger annihilation cross sections than S3M models because of the  $\bar{X}X \rightarrow \bar{q}q$  channel (see Fig. 4e and 4f), which is helicity suppressed for scalar mediators because they do not carry spin, resulting in higher predicted DM masses (and mass splittings) in perturbative calculations.

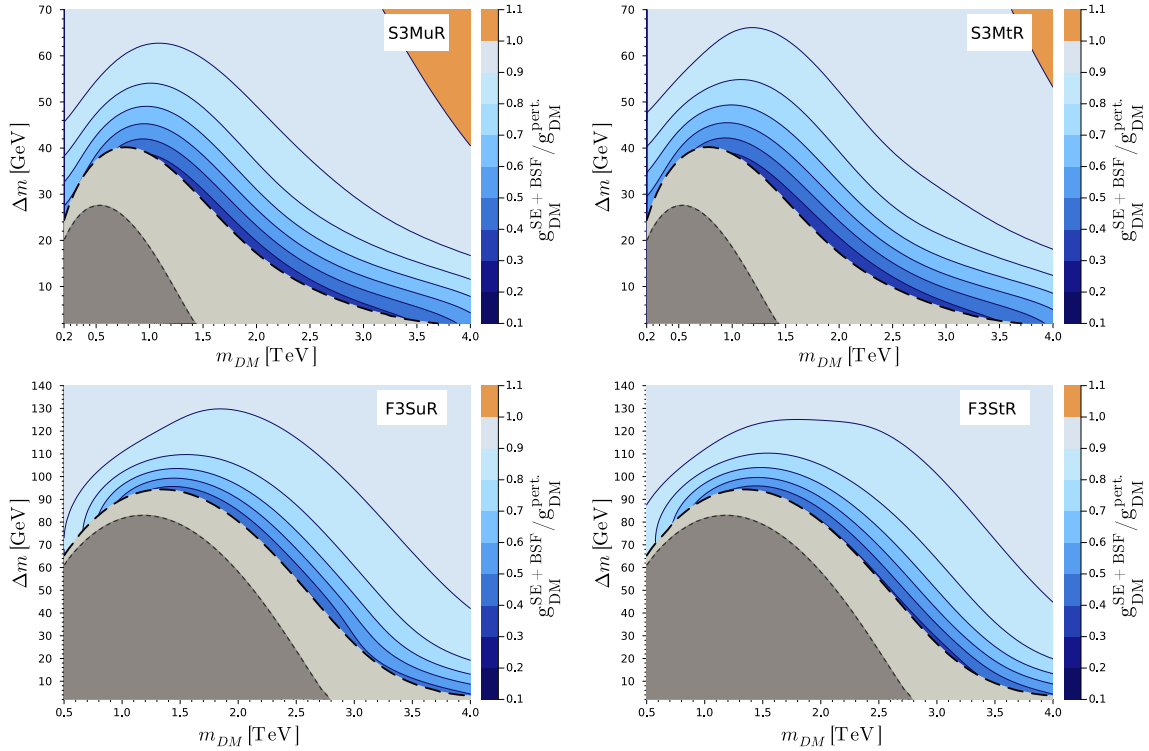


FIG. 3: Ratio of Yukawa couplings  $g_{DM}$  for which  $\Omega h^2 = 0.12$  with and without non-perturbative effects. Blue contours indicate a smaller value of  $g_{DM}$  required to satisfy the relic density constraint when long-range effects are included, while orange contours indicate the opposite. The gray areas indicates the regime of non thermal DM. In dark gray, the corresponding regime without including long-range effects is shown, while the light gray region indicates the same regime taking into account long-range effects.

- Sommerfeld effect: F3S models show a stronger impact of from the Sommerfeld enhancement at large  $g_{DM}$  (compare the off-

set between the blue dash-dotted and blue dashed curves in the upper panel (S3M) and lower panel (F3S) in Fig. 2), as now also the

unsuppressed  $\bar{X}X \rightarrow \bar{q}q$  channels (see Fig. 4e and 4f) are enhanced by the Sommerfeld effect.

- Bound State Formation (BSF) contributes similarly for both scalar and fermionic mediators. However, for fermionic mediators, there is an additional consideration related to spin. The fermionic mediator pair can form both spin-singlet and spin-triplet bound states. At late times, after chemical freeze-out, when bound states decay faster than they are ionized by thermal photons, the spin-triplet states contribute more strongly to the annihilation rate. However, such late

times are not directly impacting the freeze-out abundance. Despite this potential enhancement in the late universe, the overall impact of BSF on the relic density is actually smaller for fermionic mediators than for scalar mediators. This is because fermionic models already have larger perturbative annihilation cross sections (as explained earlier), so the relative enhancement from BSF is reduced. This comparative effect is visible in the offset between the dash-dotted (perturbative only) and solid (including BSF) curves in Fig. 2, where the offset is smaller for fermionic mediators (lower panel) than for scalar mediators (upper panel).

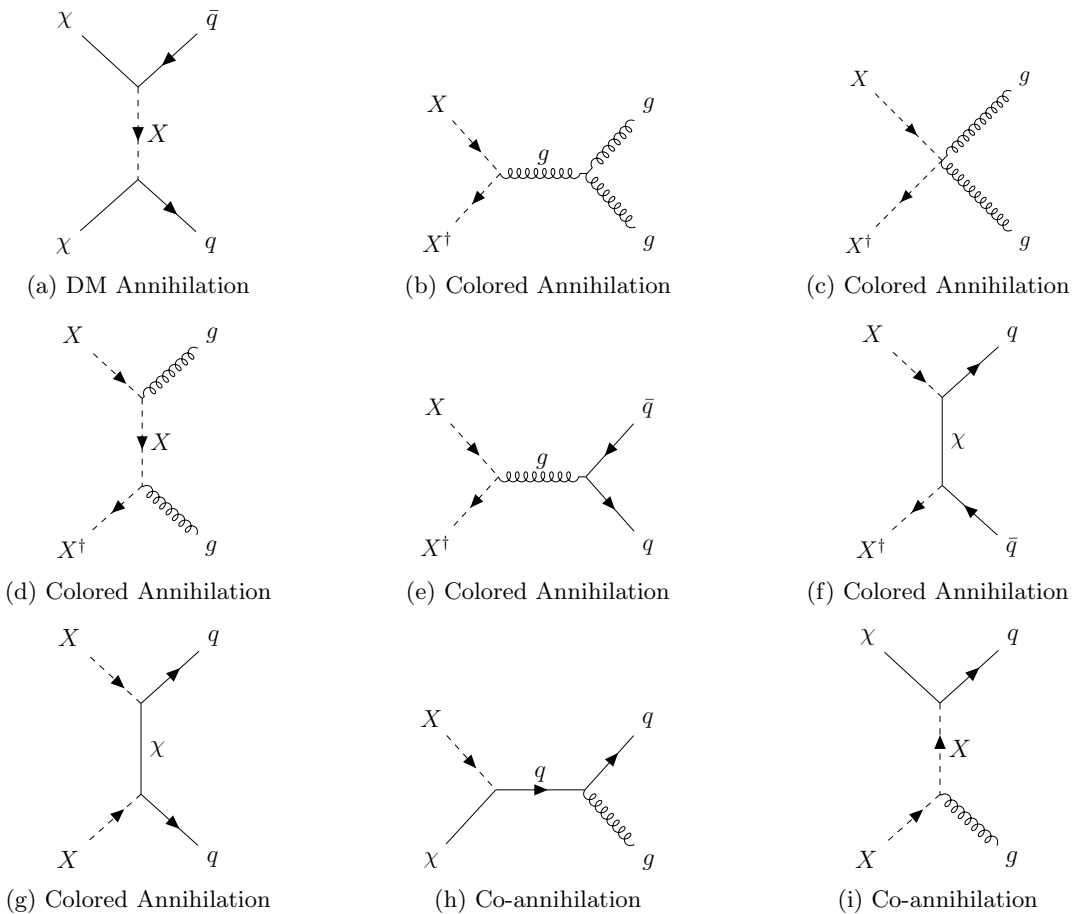


FIG. 4: Representative Feynman diagrams corresponding to the main processes contributing to (co-)annihilations. From Ref. [47].

For the **S3MuR**, **S3MtR** and **F3StR** models one observes a step increase of the  $g_{\text{DM}} = 1$  bands (see Fig. 2). This is because, for low  $m_{\text{DM}}$ ,  $\chi$  annihilations mediated by  $g_{\text{DM}}$  dominate  $\langle\sigma v_{\text{rel}}\rangle$  and mediator (co-)annihilation becomes almost irrelevant (diagram 4a dominates) such that the relic density is practically independent of  $m_X$  for  $\Delta m \lesssim m_{\text{DM}}$ . This is the case for all the plots we show in this paper. For the **F3SuR** model, this feature appears for masses  $m_{\text{DM}} < 200$  GeV or for higher values of  $g_{\text{DM}}$ , because the  $\bar{X}X \rightarrow \bar{q}q$  annihilations (diagrams 4e and 4f) neither experience a phase space suppression (like in the **F3StR** model due to the coupling to the massive top quark), nor are these annihilations helicity suppressed (as for the **S3** models), such that

it takes higher values of  $g_{\text{DM}}$  to become larger than the  $\alpha_s$  mediated  $\bar{X}X$  annihilations (diagrams 4b - 4d).

The impact of non-perturbative effects on the parameter space is summarized in Fig. 3, which shows the ratio of Yukawa couplings  $g_{\text{DM}}$  required to obtain the observed relic density  $\Omega h^2 = 0.12$  with and without long-range effects. When the inclusion of Sommerfeld enhancement and bound state formation lowers the required coupling, the corresponding parameter region is shown in blue, indicating an overall enhancement of the annihilation rate. Conversely, regions in orange correspond to a higher required  $g_{\text{DM}}$ , reflecting scenarios where non-perturbative effects suppress the ef-

fective cross section. The gray shaded areas denote the regime where DM is not produced via thermal freeze-out, instead DM production must proceed via conversion-driven freeze-out or freeze-in. The darker gray shows the corresponding region without considering long-range effects, while the lighter gray extension illustrates how non-perturbative processes can enlarge the boundary of the non-freeze-out regime.

As a cross-check and validation of our work we compare our results with existing literature. Ref. [46] has studied the S3MuR and F3SuR without including long-range effects and our perturbative results agree with their findings. The Sommerfeld effect has been included for S3MuR in Ref. [48], confirming the results presented in this work. The impact of the Sommerfeld effect for F3SuR has been assessed in Refs. [43, 48] and Ref. [90] studied F3StR.

Our perturbative results show perfect agreement with previous studies, while comparisons of the Sommerfeld effect for the F3S models reveal modest deviations ( $\leq 20\%$  for  $\delta \simeq 10^{-2}$ ). These differences could originate from our approximation of the color decomposition<sup>3</sup>, which may differ from that adopted in Refs. [43, 48, 90], as well as from our omission of subleading contributions such as loop corrections and three-body decays. However, importantly, these inaccuracies at small mass splitting are subleading compared to the inclusion of bound-state formation, which constitutes the dominant annihilation channel in this regime.

## B. Experimental constraints

In the following, we aim to confront the parameter space with constraints from direct detection and collider searches as summarized in Figs. 5 and 7.

In these plots, the dark matter coupling is fixed by imposing not to overproduce the relic density: the left panels show results from conventional perturbative calculations, while the right panels incorporate our refined treatment, which includes Sommerfeld enhancement and BSM.

Crucially, our refined calculation predicts lower values of the  $t$ -channel coupling  $g_{\text{DM}}$  compared to the perturbative approach, as long-range effects

mediated by  $\alpha_s$  dominate the annihilation cross-section for a sufficiently small mass splitting and  $g_{\text{DM}}$  can thus be much lower whilst reproducing the correct relic abundance (see Fig. 3). This reduction in  $g_{\text{DM}}$  significantly enlarges the allowed parameter space, reopening regions that would otherwise be excluded from direct detection experiments.

The hatched areas at high  $\Delta m$  mark the estimated breakdown of perturbative unitarity [91, 92] ( $g_{\text{DM}}^2 > 4\pi$ ), while the dark gray region indicates when chemical equilibrium in the dark sector is lost ( $\Gamma^{X \rightarrow X} \lesssim H$ ). The absence of chemical equilibrium is invalidating the treatment of using a single effective Boltzmann equation for the DM relic abundance, as discussed in Eq. (7) in Sec. II. We label this area as the **No Freeze-Out** region in our plots.

Importantly, this region remains *unconstrained* by direct detection experiments due to the extremely small values of  $g_{\text{DM}} \lesssim 10^{-7}$  — insufficient to produce detectable nuclear recoils. Instead, collider searches for long-lived particles become the primary probe in the gray region, as explored in Refs. [47, 50, 76, 93]. In the following we discuss the experimental limits arising from the search for bound state resonances as well as direct detection experiments shown in Figs. 5 and 7 in more detail. We summarize how their interpretation is altered when the Sommerfeld effect and bound state formation are considered.

### 1. Bound State Searches at the LHC

Dark Matter mediator masses  $m_X = m_{\text{DM}} + \Delta m$  can be probed at colliders through resonant diphoton searches. When produced at the LHC, mediator pairs ( $\tilde{X}X$ ) may form bound states that decay predominantly into gluons — which is the dominant decay channel for the relic density calculations — but also into photons, albeit with a much smaller branching fraction, irrelevant for the effective BSM cross section ( $\frac{\Gamma(\mathcal{B}(\tilde{X}X) \rightarrow \gamma\gamma)}{\Gamma(\mathcal{B}(\tilde{X}X) \rightarrow gg)} = \frac{9}{8} \frac{\alpha_{\text{QED}}^2}{\alpha_s^2} \sim \mathcal{O}(10^{-3})$ , [94]). However, the diphoton channel offers superior sensitivity due to its cleaner experimental signature [47, 95]. We derive constraints on  $m_X$  by applying ATLAS diphoton search results [96], following the methodology of Refs. [47, 94, 95]. The production cross section for a bound state  $\mathcal{B}$  is given by [94]

$$\sigma(pp \rightarrow \mathcal{B}) = \frac{\pi^2}{8m_{\mathcal{B}}^2} \Gamma(\mathcal{B} \rightarrow gg) P_{gg} \left( \frac{m_{\mathcal{B}}}{13 \text{ TeV}} \right) \quad (47)$$

<sup>3</sup> The color decomposition that we employ is detailed in Appendix A.

where  $P_{gg}$  is the two gluon luminosity. This production cross section holds for one bound state made out of scalars. For couplings to  $n_f$  flavors of quarks, the limits are  $n_f$  times stronger because of the flavor universal QCD coupling. On the other hand, bound states made out of fermions have a production cross section suppressed by  $1/4$ , as only the spin singlet state decays into two gauge bosons. For these two reasons, we only obtain limits for the **S3MuR** and **S3MtR** models for  $200 \text{ GeV} \lesssim m_B \lesssim 450 \text{ GeV}$  (see the blue areas in the lower left corners in Fig. 5). It is important to emphasize that these limits are independent of the  $t$ -channel coupling  $g_{\text{DM}}$ , provided the condition  $\Gamma_X \lesssim E_B$  is satisfied. Thus, they also apply to any dark matter production mechanism within the gray **No Freeze-Out** region. In this context, we stress that conventional resonant searches can still yield valuable insights for this class of models, potentially bridging the gap between prompt and long-lived particle searches. For more details and the demonstration of their impact in the parameter space we refer the reader to Ref. [47].

## 2. Direct Dark Matter Detection

To obtain limits from direct dark matter detection experiments, we calculate the DM-nucleon cross section using the standard effective field theory (EFT) for Majorana and real scalar DM found in the literature [44, 97–102]. The effective Lagrangian for fermionic DM relevant to our discussion is given by<sup>4</sup>

$$\begin{aligned} \mathcal{L}_{\text{eff}} = & \sum_{q=u,d} \tilde{c}_q (\bar{\chi} \gamma^\mu \gamma_5 \chi) (\bar{q} \gamma_\mu \gamma_5 q) \quad (48) \\ & + \sum_{q=u,d,s} f_q m_q \bar{\chi} \chi \bar{q} q + f_G \frac{\alpha_s}{\pi} G_{\mu\nu}^a G^{a\mu\nu} \\ & + \sum_{q=u,d,s} \left( g_1^q \frac{\bar{\chi} i \partial^\mu \gamma^\nu \chi}{m_{\text{DM}}} + g_2^q \frac{\bar{\chi} (i \partial^\mu) (i \partial^\nu) \chi}{m_{\text{DM}}^2} \right) \mathcal{O}_{\mu\nu}^q. \end{aligned}$$

The first term in Eq. (48) induces a spin-dependent (SD) coupling for fermionic DM<sup>5</sup> coupled to first

<sup>4</sup> The corresponding terms for scalar DM look the same but all coefficients for operators involving  $\gamma$  matrices vanish.

<sup>5</sup> Since scalar DM carries no spin, SD DM-nucleon interactions can only arise with a velocity suppression.

generation quarks. Thus, of the four models discussed in this paper, this operator is only active for **S3MuR**, excluding the purple area in the upper row of Fig. 5 and Fig. 6. The first term in the second line is the quark matching coefficient, while the second term constitutes the gluon matching coefficient. Finally, the operator  $\mathcal{O}_{\mu\nu}^q$  in the third line is the *quark twist-2 operator*. For the **F3S** models (scalar DM), the first of the two quark twist-2 coefficients and the spin-dependent tree level interaction are absent:  $g_1^q = \tilde{c}_q = 0$ .

We adopt the conventions of Ref. [99] and split the gluonic matching coefficient  $f_G$  into long distance (LD) - and short distance (SD) contributions<sup>6</sup>,

$$f_G = \sum_{q=u,d,s,c,b,t} f_G^{(q)} \Big|_{\text{SD}} + \sum_{Q=c,b,t} f_G^{(Q)} \Big|_{\text{LD}}, \quad (49)$$

thereby correctly disentangling contributions stemming from light quarks ( $u, d, s$ ) into perturbative ones (accounted for in the matching coefficients) and non-perturbative ones (captured already at the level of the tabulated nuclear matrix elements [103]).

As pointed out in Ref. [102], Higgs-penguin contributions to the gluon matching coefficient  $f_G$  can be relevant for models coupling to top quarks and we include them in our analysis,<sup>7</sup> using the relation given in Ref. [101].

We do not, however, include contributions from the anapole moment [104] to the **S3M** models or employ an RG improvement on the Wilson coefficients of the DM-nucleon EFT [44], as these refinements are beyond the scope of this paper and we deem their impact to be small for the following reasons:

- For simplified  $t$ -channel DM models, the anapole moment is typically velocity suppressed and thus subleading [50].
- For real scalar DM, the RG evolution down to the nucleon scale has been discussed in [105]

<sup>6</sup> The acronym SD is standard at the same time for *spin-dependent* and *short distance* in the direct detection literature. However, in a given context there is little potential for confusion.

<sup>7</sup> Readers should be aware that some expressions in Ref. [102] display inconsistent mass dimensionality. Though often correctable via dimensional analysis, we encountered multiple instances requiring explicit correction during our implementation.

(without applications to direct detection limits, as the focus of this work was the EFT operator basis up to dimension 7). The RG improvement in the direct detection of Majorana DM has been worked out in Ref. [44] and it has been found that in particular  $f_G$  receives large corrections of order  $\mathcal{O}(\alpha_s)$ . However, our work differs with respect to Ref. [44] in the way we define our effective operator to gluons. Crucially, following the convention of Ref. [101], we explicitly include a factor of  $\alpha_s$  in the *definition* of the operator coupling to gluons (whereas  $\alpha_s$  is not part of the definition of the corresponding operator in Ref. [44]), which renders the operator defined in our convention manifestly RG invariant:  $\mu \frac{d}{d\mu} \frac{\alpha_s}{\pi} G_{\mu\nu}^a G^{a\mu\nu} = 0$ . This convention automatically includes the running of the operator in its definition, such that an additional RG improvement is not needed in our setup.

Moreover we neglect gluon twist-2 operators, as these operators are suppressed with one order of  $\alpha_s$  compared to the DM-gluon effective operator mediated by  $f_G$  [99].

We obtain direct detection bounds on our models by comparing the SD and SI cross sections to the recent limits of the LUX-ZEPLIN (LZ) experiment [106]:

- For **S3MuR**, the most constraining limits (shown in the upper rows of Figs. 5 and 6) stem from the SD scattering, while the SI limits are driven by the up-quark twist-2 contributions  $g_1^q + g_2^q$  [44, 99, 102].
- The constraints for the **S3MtR** model (shown in the lower rows of Figs. 5 and 6) have a different origin: The Higgs-penguin contribution is essentially independent of  $\Delta m$  [102], while the DM-gluon effective interaction strongly decreases with larger  $\Delta m$  [99]. Thus, the DM-gluon effective interaction causes the

limits for  $\Delta m \lesssim 250$  GeV, where the upper excluded region stems from the aforementioned loop-induced Higgs penguin contribution.

- The **F3SuR** model is almost completely excluded by direct detection (as can be seen in the upper rows of Figs. 7 and 8), where - as in the case of **S3MuR** - the biggest contribution stems from the quark twist-2 coefficient  $g_2^q$ . Apart from the unconstrained **No Freeze-Out** region, there is only a small area in the upper right corner that is not excluded, as for high masses both the experimental sensitivity and the quark twist-2 coefficient  $g_2^q$  is smaller.
- Finally, **F3StR**, displayed in the lower rows of Figs. 7 and 8, is constrained by the Higgs penguin contribution to both the  $f_q$  and  $f_G$  Wilson coefficients and by gluon loops contributing to  $f_G$  [102], leading to a connected excluded area.

Direct detection severely constrains the viable parameter space across all four models. However, including long-range effects (the right panels of Figs. 5-8) enlarges the gray, unconstrained **No Freeze-Out** region significantly. This enlargement of the theoretically allowed parameter space at weak coupling represents the key impact of long-range effects in our analysis.

When including Sommerfeld effect and BSF, parameter space is reopened, particularly in the strongly coannihilating (small  $\Delta m$ ) regime. Most strikingly, the upper mass limits from direct detection (the largest allowed  $m_{\text{DM}}$  values for  $\Delta m \rightarrow 0$  in Figs. 5-8) shift by a significant amount:

- **S3MuR**: 1.4 TeV  $\rightarrow$  4.0 TeV
- **S3MtR**: 2.8 TeV  $\rightarrow$  4.6 TeV
- **F3SuR**: 1.6 TeV  $\rightarrow$  4.0 TeV
- **F3StR**: 3.0 TeV  $\rightarrow$  5.0 TeV

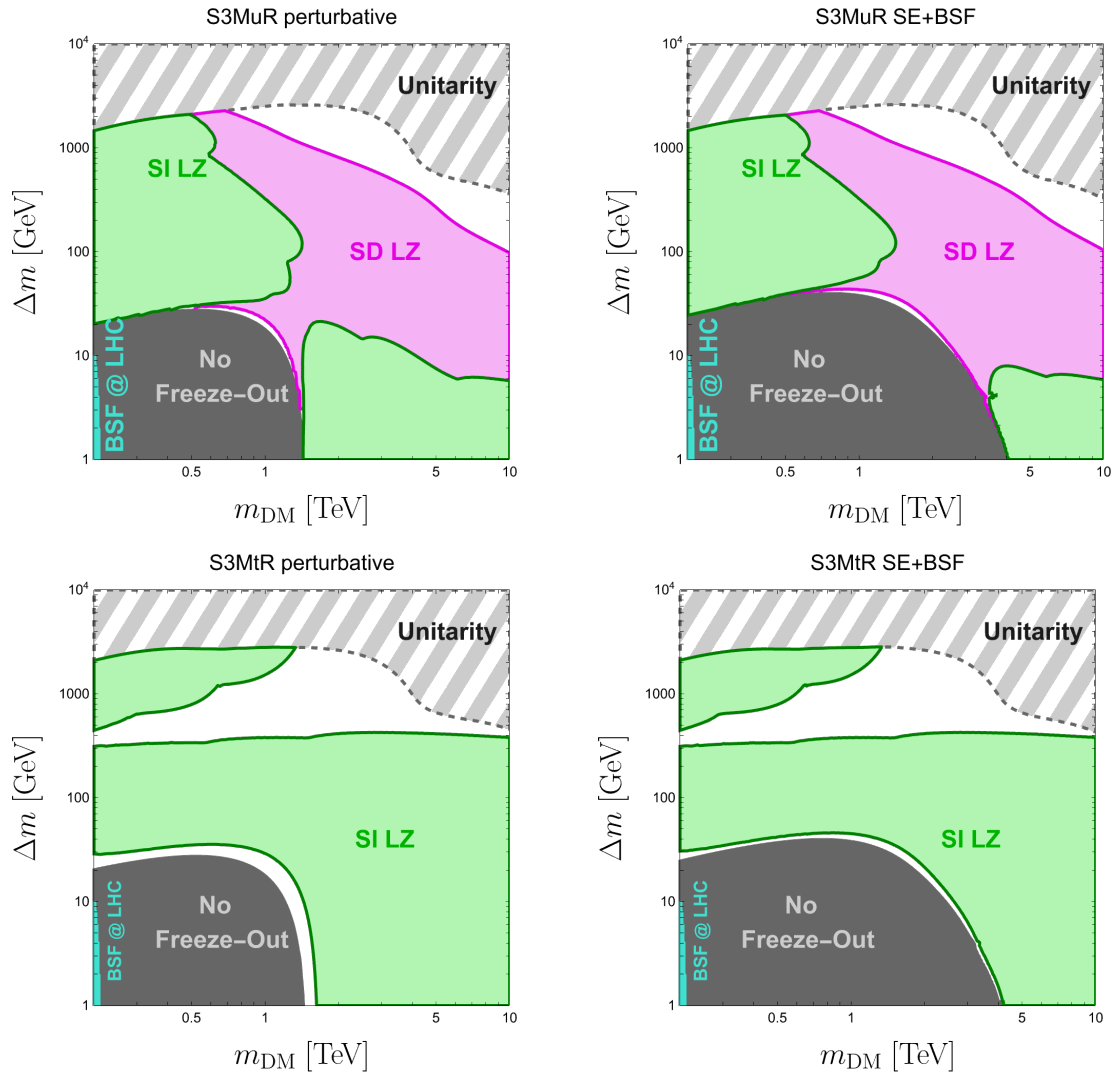


FIG. 5: Experimental bounds on the S3M models with Majorana Dark Matter and a complex scalar mediator. The upper row is for the models coupling to the up-quark, the lower for couplings to the top. The left column shows the constraints without long-range effects, while the right column includes them.

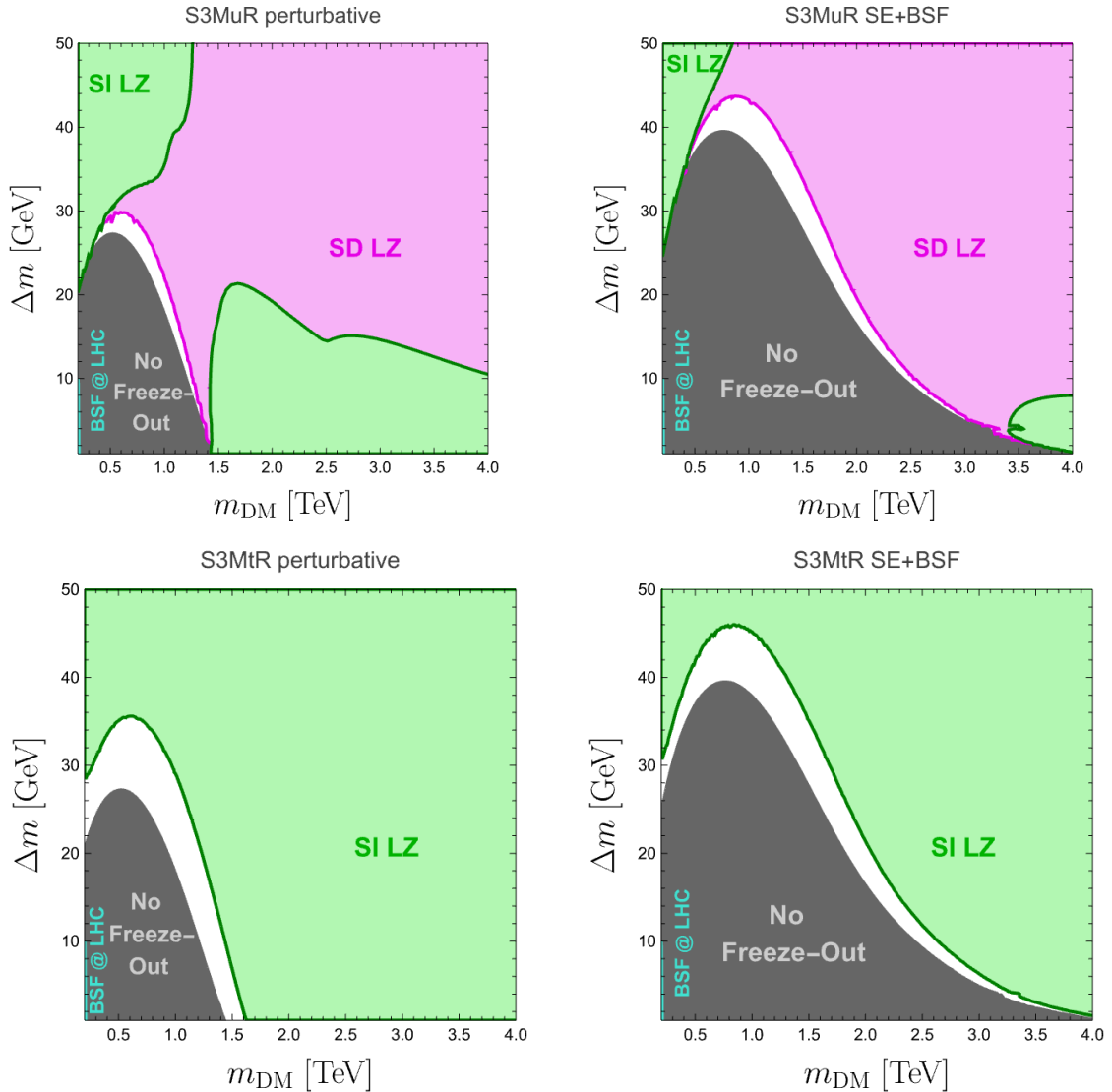


FIG. 6: Same as Fig. 5, but plotted on a linear Dark Matter mass axis. Experimental bounds on the S3M model with Majorana Dark Matter and a complex scalar mediator, showing couplings to up quarks (upper row) and top quarks (lower row), without (left) and with (right) long-range effects.

These shifts - up to nearly 3 TeV in mass - highlight the importance of including long-range interactions in the phenomenology of DM. Consequently, we find an expanded viable parameter space for the S3MuR, S3MtR, and F3StR models. This under-

scores that earlier constraints, derived from perturbative treatments or from including only the Sommerfeld effect, were overly restrictive for these scenarios. In contrast, the impact on the already strongly constrained F3SuR model is negligible.

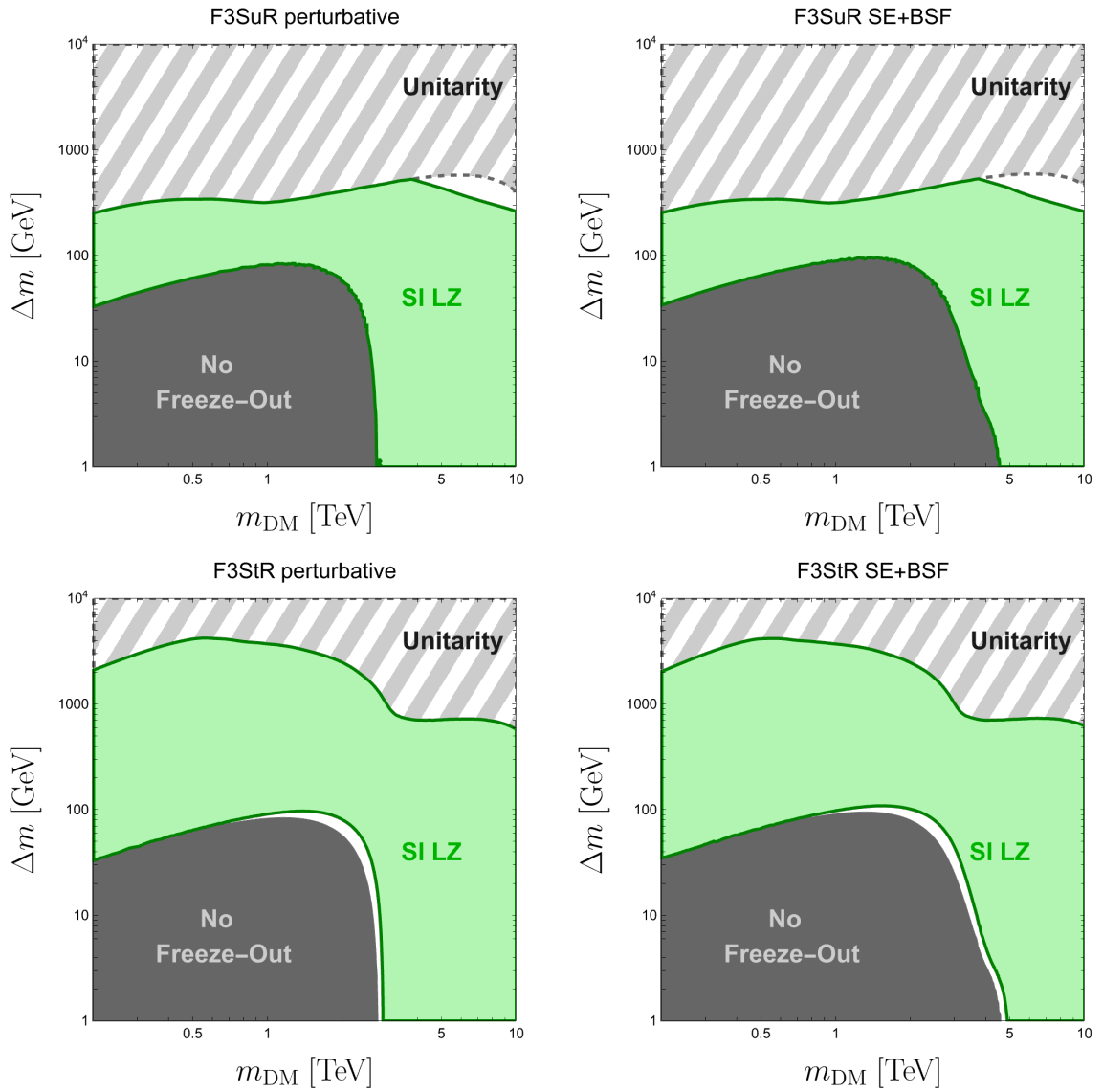


FIG. 7: Experimental bounds on the F3S models with real scalar Dark Matter and a Dirac fermionic mediator. The results are presented as in Fig. 5.

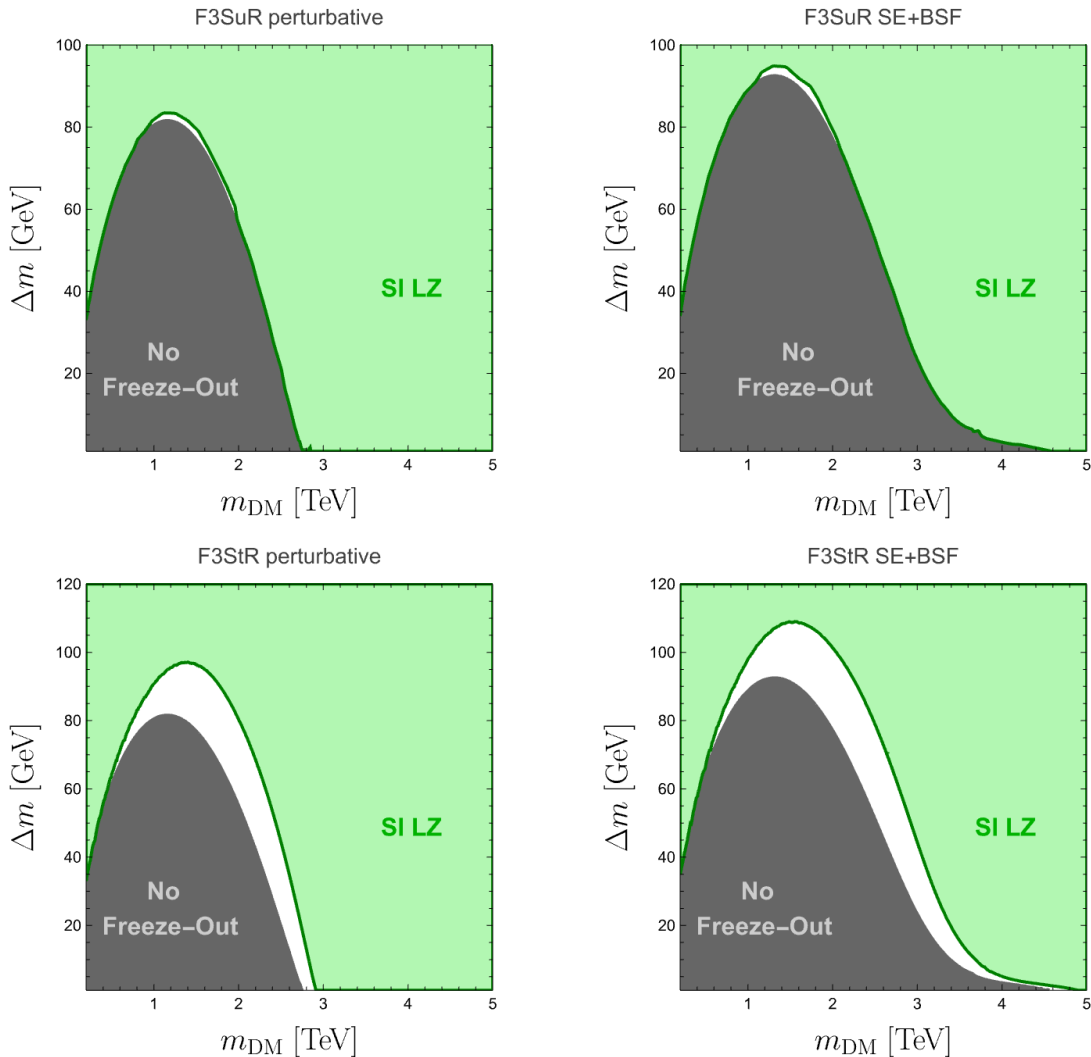


FIG. 8: Fig. 7, but plotted on a linear Dark Matter mass axis. Experimental bounds on the F3S model with real scalar Dark Matter and a Dirac fermion mediator, showing couplings to up quarks (upper row) and top quarks (lower row), without (left) and with (right) long-range effects.

Our results demonstrate that a consistent treatment of non-perturbative effects is essential for accurate predictions in this class of models.

## V. SUMMARY

Dark matter models with QCD-charged coannihilation partners remain among the most compelling and testable thermal relic scenarios. In such models, long-range effects, such as the Sommerfeld enhancement and bound state formation,

can significantly modify the annihilation dynamics in the early universe, particularly in regions with small mass splittings where coannihilation is efficient. These effects alter the relic abundance and thereby also impact the interpretation of collider and direct detection limits with respect to the viable parameter space. To quantify these effects precisely, we analyzed four representative benchmark models involving scalar or fermionic mediators coupled to either light or heavy quarks. In all cases, we find that including long-range effects leads to substantial shifts in the predicted dark matter–Standard Model  $t$ -channel coupling, when the dark matter and mediator masses are nearly degenerate. Consequently, the resulting experimental limits—particularly from direct detection—can change significantly, and upper bounds on the dark matter mass in the coannihilating regime are increased by factors of order unity. To facilitate broader application of these insights, we developed **SE+BSF4DM**, a package linked to **micrOMEGAs**, which enables an intuitive and easy-to-use precision calculation of the relic density including the Sommerfeld effect and bound state formation for QCD charged dark sector models. Thanks to its simple structure, the tool integrates seamlessly into standard dark matter phenomenology pipelines and is available via [GitHub](#).

## ACKNOWLEDGEMENTS

We thank Alexander Pukhov for his support concerning the implementation in **micrOMEGAs** and Tanushree Bhattacharya for collaboration in initial stages of this project during her internship at the University of Mainz. M. N thanks Merlin Reichard for useful input on the code and Dipan Sengupta, Sreemanti Chakraborti, Stefan Lederer and David Cabo Almeida for fruitful discussions.

The authors would like to express special thanks to the Mainz Institute for Theoretical Physics (MITP) of the Cluster of Excellence PRISMA<sup>+</sup> (Project ID 390831469), for its hospitality and support. M. B., E. C. and J. H. acknowledge support from the Emmy Noether grant “Baryogenesis, Dark Matter and Neutrinos: Comprehensive analyses and accurate methods in particle cosmology” (HA 8555/1-1, Project No. 400234416) funded by the Deutsche Forschungsgemeinschaft (DFG, German Research Foundation). M. N. acknowledges support from the DFG Collaborative Research Centre “Neutrinos,

Dark Matter and Messengers” (SFB 1258). M. B., E. C. and J. H. acknowledge support by the Cluster of Excellence “Precision Physics, Fundamental Interactions, and Structure of Matter” (PRISMA<sup>+</sup> EXC 2118/1) funded by the DFG within the German Excellence Strategy (project No. 390831469). This work was supported by Istituto Nazionale di Fisica Nucleare (INFN) through the Theoretical Astroparticle Physics (TAsP) project, and in part by the Italian MUR Departments of Excellence grant 2023-2027 “Quantum Frontiers”. The work of M.B. was supported in part by the Italian Ministry of University and Research (MUR) through the PRIN 2022 project n. 20228WHTYC (CUP:I53C24002320006 and C53C24000760006).

## Appendix A: Color decomposition

This appendix contains further details on the employed color decomposition for scalar and fermionic mediators, which constitute the ‘default’ settings implemented in our package. The coefficients  $c_{\ell s}^{[\mathbf{R}]}$  of Eq. (16) for an arbitrary  $2 \rightarrow 2$  process are given by:

$$c_{\ell s}^{[\mathbf{R}]} = \frac{1}{|\mathcal{M}_{\text{full}}|^2} \left| \frac{2\ell + 1}{2} \int_{-1}^1 d(\cos \theta) P_{\ell}(\cos \theta) P^{[\mathbf{R}]} \mathcal{M}_{\text{full}}^s \right|^2, \quad (\text{A1})$$

where  $P_{\ell}(\cos \theta)$  are the Legendre polynomials of the first kind that project out the  $\ell$ -th partial wave,  $P^{[\mathbf{R}]}$  is the projector onto the  $SU(3)_c$  representation  $\mathbf{R}$  and  $\mathcal{M}_{\text{full}}^s$  is the perturbative matrix element in a total spin  $s$  configuration (to arbitrary loop order). As elaborated in the main text, we will simplify the analysis by keeping only the  $v_{\text{rel}}^0$  contribution, thereby automatically singling out solely contributions to the s-wave. Thus one obtains

$$c_{0s}^{[\mathbf{R}]} = \frac{\sigma_{0s}^{[\mathbf{R}]}}{\sigma_0}, \quad (\text{A2})$$

$$\mathcal{S}(\sigma) \simeq \sum_{[\mathbf{R}]} S_0^{[\mathbf{R}]} \sum_s c_{0s}^{[\mathbf{R}]} \sigma_{0s}. \quad (\text{A3})$$

Explicitly, this implies that we only keep the  $l = 0$  and  $v_{\text{rel}} \rightarrow 0$  terms in Eq. (16). Thus, the

following coefficients are employed in our code:

$$\mathcal{S}(\sigma_{XX^\dagger \rightarrow g\mathcal{A}}) = S_0^{[\mathbf{8}]} \sigma_{XX^\dagger \rightarrow g\mathcal{A}}, \quad (\text{A4})$$

$$\mathcal{S}(\sigma_{XX^\dagger \rightarrow \mathcal{B}\mathcal{C}}) = S_0^{[\mathbf{1}]} \sigma_{XX^\dagger \rightarrow \mathcal{B}\mathcal{C}}, \quad (\text{A5})$$

$$\begin{aligned} \mathcal{S}(\sigma_{XX^\dagger \rightarrow gg}) &\simeq \left( \frac{2}{N_c^2 - 2} S_0^{[\mathbf{1}]} \right. \\ &\quad \left. + \frac{N_c^2 - 4}{N_c^2 - 2} S_0^{[\mathbf{8}]} \right) \sigma_{XX^\dagger \rightarrow gg}, \quad (\text{A6}) \end{aligned}$$

$$\begin{aligned} \mathcal{S}(\sigma_{X_i^\dagger X_j \rightarrow \bar{q}_i q_j}) &\simeq \\ &\sigma_{X_i^\dagger X_j \rightarrow \bar{q}_i q_j} \times \begin{cases} S_0^{[\mathbf{8}]} , X \text{ fermionic} \ \& \ i = j \\ \frac{1}{N_c^2} S_0^{[\mathbf{1}]} + \frac{N_c^2 - 1}{N_c^2} S_0^{[\mathbf{8}]} , \text{ else} \end{cases}, \quad (\text{A7}) \end{aligned}$$

$$\begin{aligned} \mathcal{S}(\sigma_{X_i X_j \rightarrow q_i q_j}) &\simeq \\ &\sigma_{X_i X_j \rightarrow q_i q_j} \times \begin{cases} S_0^{[\mathbf{6}]} , X \text{ scalar} \ \& \ i = j \\ \frac{N_c - 1}{2N_c} S_0^{[\mathbf{3}]} + \frac{N_c + 1}{2N_c} S_0^{[\mathbf{6}]} , \text{ else} \end{cases}. \quad (\text{A8}) \end{aligned}$$

A few comments to these equations are in order:

- The particle  $\mathcal{A}$  in Eq. (A4) is a color-neutral SM vector boson  $\mathcal{A} = \{A, W^\pm, Z\}$ .
- In Eq. (A5), the particles  $\mathcal{B}$  and  $\mathcal{C}$  represent any color neutral particle of the SM:  $\mathcal{B}, \mathcal{C} = \{A, W^\pm, Z, h, \ell\}$ .
- The relation Eq. (A6) is exact for the s-wave part. One might expect different coefficients for fermionic  $X$  particles, as they can be in spin singlet or triplet configurations. That the spin triplet does not appear in Eq. (A6) is a manifestation of the Landau-Yang theorem, according to which a (color-neutral) massive spin 1 state cannot decay into two massless spin 1 particles.
- For the process described in Eq. (A7), there are two competing diagrams: one is a  $t$ -channel DM exchange mediated by  $g_{\text{DM}}$ , the

other are s-channel SM gauge boson exchanges, in particular gluons. Due to interferences between these diagrams, the coefficients formally depend on all the masses and couplings of the particles involved in the process. The decomposition Eq. (A7) holds for the s-wave part and in the limit  $g_{\text{DM}}^2/\alpha_s \rightarrow 0$ , introducing a theoretical error of  $\mathcal{O}\left(\frac{g_{\text{DM}}^4}{4\pi^2(N_c^2-1)\alpha_s^2}\right)$ . We assume this limit of this particular Sommerfeld coefficient as the default setting in our code since long-range QCD effects are mostly of interest when colored annihilations dominate the annihilation cross section.

- In equation Eq. (A8), the annihilation of scalars into two identical quarks represents a special situation where the symmetry of the wavefunction forbids a contribution of the (antisymmetric)  $[\mathbf{3}]$  channel for  $\ell = 0$ .

Equations with an = sign are exact, while those with an  $\simeq$  sign only hold in certain limits, as indicated above. We state the general results for an  $SU(N_c)$  group here, while in the code we explicitly set  $N_c = 3$ . Following the discussion of Appendix B, the user can change these coefficients manually in the code by modifying the `SommerfeldFactor_BSMmodel` function.

### Appendix B: micrOMEGAs package for Sommerfeld effect and bound state formation

For a full manual, we refer the reader to Ref. [107]. In practice, the code will go through all possible coannihilating pairs of dark sector particles and calculates the contributions of Sommerfeld effect and BSF in case the pair belongs to a  $\mathbf{3} \otimes \bar{\mathbf{3}}$  or  $\mathbf{3} \otimes \mathbf{3}$  color configuration of QCD (see also App. A).

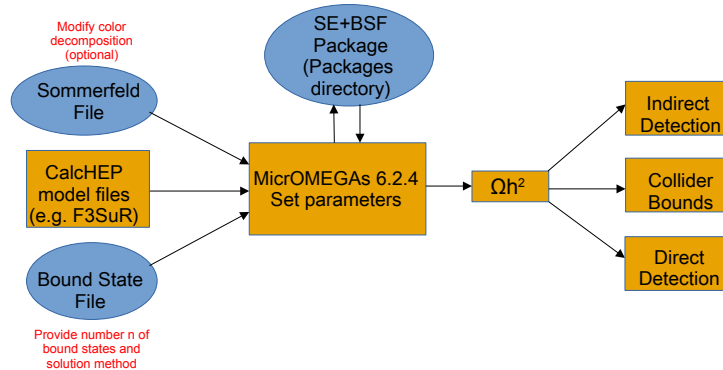


FIG. 9: Schematic workflow of the files needed to be included for the SE+BSF4DM package.

Within an ordinary `micrOMEGAs` installation, our package can be included by downloading the publicly available files from our [Github](#) project page. The directory `SE_BSF` containing the files `SE_BSF_header.h` and `SE_BSF_functions.cpp` has to be downloaded into the `Packages` directory of `micrOMEGAs`. These files contain all the model-independent definitions and functions needed for evaluating the expressions presented in Sec. III. We stress that our package requires no modifications to the `micrOMEGAs` source code and integrates seamlessly into existing installations. It extends `micrOMEGAs` capabilities to include long-range effects while maintaining all of `micrOMEGAs` original features.

Once a new model is defined in `micrOMEGAs`, e.g. `F3StR`, a new directory with the same name is created in the main `micrOMEGAs` folder. To include long-range effects for the newly generated model, the two files `improveCrossSectionSommerfeld.cpp` and `BoundStateFormation.cpp` must be added to the `F3StR/lib/` directory. These files need to be customized to the user’s need:

- In the file `improveCrossSectionSommerfeld.cpp` the user can turn the Sommerfeld effect on or off with the flag `int somm_flag` (off: `somm_flag = 0`, on: `somm_flag = 1`). In the following nested `if` block in the function `SommerfeldFactor_BSMmodel`, the prede-

finer factor `kQfac` corresponding to  $c_{\ell s}^{[R]}$  in Eq. (A1) for the various processes described in Appendix A are given. These coefficients can be altered or new coefficients can be added (e.g. for  $8 \otimes 8$ ) using a new `if ...` block. If the default settings (Eqs. (A4) - (A8) in Appendix A) shall be used, no further action is required. The function `improveCrossSection` is located in the same file and it is used for our user-defined Sommerfeld factors. This function was originally created by the `micrOMEGAs` developers to enable the user to modify the tree-level cross section for a given process (e.g. by adding loop corrections through the software package `DM@NLO` [12, 24, 58, 60–64]) and we have repurposed it for the Sommerfeld effect. In case the user wants to use this original functionality, they can do so by implementing the desired modifications (loop corrections) in a new `else if (somm_flag==2){...}` environment.

- In the file `lib/BoundStateFormation.cpp` the user can define the specifications of how BSF should be implemented in `micrOMEGAs`. Four lines are necessary to be specified by the user:

1. `int bsf_scenario = 0,1,2,3,4` specifies the treatment of BSF, corresponding respectively to: no BSF, the no-transition limit, the

efficient-transition limit, ionization equilibrium, or the full solution (see Sec. III C). Setting this flag to 0 disables BSF.

2. `num_excited_states=n` includes bound states with main quantum number up to  $n$ . Setting `n=0` turns off BSF.
3. `const int num_of_mediators` sets the number of colored particles in the dark sector.
4. `int pdg_nums_mediators` is an array with length `[num_of_mediators]` containing the PDG numbers for the colored particles in the dark sector.

Finally, in the `F3StR/main.cpp` file, one needs to include the two aforementioned files with

```
#include "lib/
  improveCrossSection_Sommerfeld
  .cpp"
#include "lib/BoundStateFormation
  .cpp"
```

After these steps, the Sommerfeld effect and BSF are included in the calculation of the relic abundance, according to the users specifications defined in the two files in the `F3StR/lib/` folder

and `micrOMEGAs` can be used as usual. The relic density is calculated with

```
Omega = darkOmegaExt(&Xf,
  BSF_XS_A, BSF_XS_S);
```

instead of the usual `darkOmega` routine. In the current release, our code includes the Sommerfeld effect and BSF in the **coannihilation regime**, i.e. where  $g_{DM}$  is sufficiently large to maintain chemical and kinetic equilibrium in the dark sector (see the discussion in Sec. II). We note that there is no check and corresponding warning if a parameter point analyzed does not maintain chemical equilibrium in the dark sector and it remains the task of the user to make sure that this condition is satisfied. Incorporating also the **freeze-in** and **conversion-driven freeze-out** regimes, where excited states have been shown to play a pivotal role [77, 78], is straightforward, but requires additional functionalities of `micrOMEGAs`. In particular a new function `darkOmegaExt`, which is a fusion of `darkOmegaExt` and `darkOmegaN`, allowing for a user-defined cross-section for dark matter models in the cospattering regime [108], would be desirable. We are in contact with the `micrOMEGAs` developers and this will be the focus of a follow-up work.

- 
- [1] J. Aalbers *et al.* (LZ), *Phys. Rev. Lett.* **131**, 041002 (2023), [arXiv:2207.03764 \[hep-ex\]](#).
  - [2] E. Adams *et al.* (PICO), *Phys. Rev. D* **108**, 062003 (2023), [arXiv:2301.08993 \[astro-ph.CO\]](#).
  - [3] E. Aprile *et al.* (XENON), *Eur. Phys. J. C* **84**, 784 (2024), [arXiv:2402.10446 \[physics.ins-det\]](#).
  - [4] G. Arcadi, M. Dutra, P. Ghosh, M. Lindner, Y. Mambrini, M. Pierre, S. Profumo, and F. S. Queiroz, *Eur. Phys. J. C* **78**, 203 (2018), [arXiv:1703.07364 \[hep-ph\]](#).
  - [5] T. Abe *et al.* (LHC Dark Matter Working Group), *Phys. Dark Univ.* **27**, 100351 (2020), [arXiv:1810.09420 \[hep-ex\]](#).
  - [6] A. M. Sirunyan *et al.* (CMS), *JHEP* **03**, 025, [arXiv:1908.01713 \[hep-ex\]](#).
  - [7] G. Aad *et al.* (ATLAS), *Sci. Bull.* **69**, 3005 (2024), [arXiv:2306.00641 \[hep-ex\]](#).
  - [8] D. Perez Adan (ATLAS, CMS), in *56th Rencontres de Moriond on Electroweak Interactions and Unified Theories* (2023) [arXiv:2301.10141 \[hep-ex\]](#).
  - [9] P. Harris, P. Schuster, and J. Zupan, in *Snowmass 2021* (2022) [arXiv:2207.08990 \[hep-ph\]](#).
  - [10] K. Griest and D. Seckel, *Phys. Rev. D* **43**, 3191 (1991).
  - [11] P. Gondolo and J. Edsjo, *Nucl. Phys. B Proc. Suppl.* **70**, 120 (1999), [arXiv:hep-ph/9711461](#).
  - [12] J. Harz, B. Herrmann, M. Klasen, K. Kovarik, and Q. L. Boule'h, *Phys. Rev. D* **87**, 054031 (2013), [arXiv:1212.5241 \[hep-ph\]](#).
  - [13] M. J. Baker *et al.*, *JHEP* **12**, 120, [arXiv:1510.03434 \[hep-ph\]](#).
  - [14] J. Ellis, K. A. Olive, and J. Zheng, *Eur. Phys. J. C* **74**, 2947 (2014), [arXiv:1404.5571 \[hep-ph\]](#).
  - [15] A. Ibarra, A. Pierce, N. R. Shah, and

- S. Vogl, *Phys. Rev. D* **91**, 095018 (2015), [arXiv:1501.03164 \[hep-ph\]](#).
- [16] S. El Hedri, A. Kaminska, M. de Vries, and J. Zurita, *JHEP* **04**, 118, [arXiv:1703.00452 \[hep-ph\]](#).
- [17] S. El Hedri and M. de Vries, *JHEP* **10**, 102, [arXiv:1806.03325 \[hep-ph\]](#).
- [18] S. Biondini and S. Vogl, *JHEP* **11**, 147, [arXiv:1907.05766 \[hep-ph\]](#).
- [19] A. Sommerfeld, *Annalen Phys.* **403**, 257 (1931).
- [20] A. D. Sakharov, *Zh. Eksp. Teor. Fiz.* **18**, 631 (1948).
- [21] M. Beneke, C. Hellmann, and P. Ruiz-Femenia, *JHEP* **03**, 162, [arXiv:1411.6930 \[hep-ph\]](#).
- [22] M. Beneke, R. Szafron, and K. Urban, *Phys. Lett. B* **800**, 135112 (2020), [arXiv:1909.04584 \[hep-ph\]](#).
- [23] J. Hisano, S. Matsumoto, M. Nagai, O. Saito, and M. Senami, *Phys. Lett. B* **646**, 34 (2007), [arXiv:hep-ph/0610249](#).
- [24] J. Branahl, J. Harz, B. Herrmann, M. Klasen, K. Kovařík, and S. Schmiemann, *Phys. Rev. D* **100**, 115003 (2019), [arXiv:1909.09527 \[hep-ph\]](#).
- [25] B. von Harling and K. Petraki, *JCAP* **12**, 033, [arXiv:1407.7874 \[hep-ph\]](#).
- [26] J. Ellis, F. Luo, and K. A. Olive, *JHEP* **09**, 127, [arXiv:1503.07142 \[hep-ph\]](#).
- [27] H. An, M. B. Wise, and Y. Zhang, *Phys. Rev. D* **93**, 115020 (2016), [arXiv:1604.01776 \[hep-ph\]](#).
- [28] P. Asadi, M. Baumgart, P. J. Fitzpatrick, E. Krupczak, and T. R. Slatyer, *JCAP* **02**, 005, [arXiv:1610.07617 \[hep-ph\]](#).
- [29] K. Petraki, M. Postma, and J. de Vries, *JHEP* **04**, 077, [arXiv:1611.01394 \[hep-ph\]](#).
- [30] S. P. Liew and F. Luo, *JHEP* **02**, 091, [arXiv:1611.08133 \[hep-ph\]](#).
- [31] M. Cirelli, N. Fornengo, and A. Strumia, *Nucl. Phys. B* **753**, 178 (2006), [arXiv:hep-ph/0512090](#).
- [32] M. Cirelli, A. Strumia, and M. Tamburini, *Nucl. Phys. B* **787**, 152 (2007), [arXiv:0706.4071 \[hep-ph\]](#).
- [33] M. Cirelli and A. Strumia, *New J. Phys.* **11**, 105005 (2009), [arXiv:0903.3381 \[hep-ph\]](#).
- [34] A. DiFranzo, K. I. Nagao, A. Rajaraman, and T. M. P. Tait, *JHEP* **11**, 014, [Erratum: *JHEP* 01, 162 (2014)], [arXiv:1308.2679 \[hep-ph\]](#).
- [35] J. Abdallah *et al.*, *Phys. Dark Univ.* **9-10**, 8 (2015), [arXiv:1506.03116 \[hep-ph\]](#).
- [36] E. Morgante, *Adv. High Energy Phys.* **2018**, 5012043 (2018), [arXiv:1804.01245 \[hep-ph\]](#).
- [37] G. Bélanger *et al.*, *JHEP* **02**, 186, [arXiv:1811.05478 \[hep-ph\]](#).
- [38] A. Belyaev, G. Cacciapaglia, J. McKay, D. Marin, and A. R. Zerwekh, *Phys. Rev. D* **99**, 115003 (2019), [arXiv:1808.10464 \[hep-ph\]](#).
- [39] A. Belyaev, G. Cacciapaglia, D. Locke, and A. Pukhov, *JHEP* **10**, 014, [arXiv:2203.03660 \[hep-ph\]](#).
- [40] T. Ghosh, C. Kelso, J. Kumar, P. Sandick, and P. Stengel, in *Snowmass 2021* (2022) [arXiv:2203.08107 \[hep-ph\]](#).
- [41] G. Arcadi, M. Lindner, and S. Profumo, *Beyond the veil: Charting wimp territories at the neutrino floor* (2025), [arXiv:2507.16987 \[hep-ph\]](#).
- [42] M. Garny, A. Ibarra, and S. Vogl, *Int. J. Mod. Phys. D* **24**, 1530019 (2015), [arXiv:1503.01500 \[hep-ph\]](#).
- [43] F. Giacchino, A. Ibarra, L. Lopez Honorez, M. H. G. Tytgat, and S. Wild, *JCAP* **02**, 002, [arXiv:1511.04452 \[hep-ph\]](#).
- [44] K. A. Mohan, D. Sengupta, T. M. P. Tait, B. Yan, and C. P. Yuan, *JHEP* **05**, 115, [Erratum: *JHEP* 05, 232 (2023)], [arXiv:1903.05650 \[hep-ph\]](#).
- [45] C. Arina, B. Fuks, and L. Mantani, *Eur. Phys. J. C* **80**, 409 (2020), [arXiv:2001.05024 \[hep-ph\]](#).
- [46] C. Arina, B. Fuks, L. Mantani, H. Mies, L. Panizzi, and J. Salko, *Phys. Lett. B* **813**, 136038 (2021), [arXiv:2010.07559 \[hep-ph\]](#).
- [47] M. Becker, E. Copello, J. Harz, K. A. Mohan, and D. Sengupta, *JHEP* **08**, 145, [arXiv:2203.04326 \[hep-ph\]](#).
- [48] C. Arina, B. Fuks, J. Heisig, M. Krämer, L. Mantani, and L. Panizzi, *Phys. Rev. D* **108**, 115007 (2023), [arXiv:2307.10367 \[hep-ph\]](#).
- [49] A. Jueid and S. Kanemura, *Phys. Rev. D* **110**, 095009 (2024), [arXiv:2402.08652 \[hep-ph\]](#).
- [50] C. Arina *et al.*, *Eur. Phys. J. C* **85**, 975 (2025), [Erratum: *Eur. Phys. J. C* 85, 1105 (2025)], [arXiv:2504.10597 \[hep-ph\]](#).
- [51] S. Biondini, L. Tiberi, and O. Panella, *JHEP* **10**, 060, [arXiv:2507.00925 \[hep-ph\]](#).
- [52] P. Olgoso, P. Paradisi, and N. Selimovic, *The dark side of a tera-z factory* (2025), [arXiv:2507.17803 \[hep-ph\]](#).
- [53] M. Backović, M. Krämer, F. Maltoni, A. Martini, K. Mawatari, and M. Pellen, *Eur. Phys. J. C* **75**, 482 (2015), [arXiv:1508.05327 \[hep-ph\]](#).

- ph].
- [54] J. Harz and K. Petraki, *JHEP* **07**, 096, [arXiv:1805.01200 \[hep-ph\]](#).
- [55] G. Belanger, F. Boudjema, A. Pukhov, and A. Semenov, *Comput. Phys. Commun.* **176**, 367 (2007), [arXiv:hep-ph/0607059](#).
- [56] T. Bringmann, J. Edsjö, P. Gondolo, P. Ullio, and L. Bergström, *JCAP* **07**, 033, [arXiv:1802.03399 \[hep-ph\]](#).
- [57] F. Ambroggi, C. Arina, M. Backovic, J. Heisig, F. Maltoni, L. Mantani, O. Mattelaer, and G. Mohlabeng, *Phys. Dark Univ.* **24**, 100249 (2019), [arXiv:1804.00044 \[hep-ph\]](#).
- [58] J. Harz, B. Herrmann, M. Klasen, K. Kovařík, and L. P. Wiggering, *Eur. Phys. J. C* **84**, 342 (2024), [arXiv:2312.17206 \[hep-ph\]](#).
- [59] M. Palmiotta, A. Arbey, and F. Mahmoudi, *Comput. Phys. Commun.* **294**, 108905 (2024), [arXiv:2211.10376 \[hep-ph\]](#).
- [60] J. Harz, B. Herrmann, M. Klasen, and K. Kovarik, *Phys. Rev. D* **91**, 034028 (2015), [arXiv:1409.2898 \[hep-ph\]](#).
- [61] J. Harz, B. Herrmann, M. Klasen, K. Kovařík, and M. Meinecke, *Phys. Rev. D* **91**, 034012 (2015), [arXiv:1410.8063 \[hep-ph\]](#).
- [62] J. Harz, B. Herrmann, M. Klasen, K. Kovarik, and P. Steppeler, *Phys. Rev. D* **93**, 114023 (2016), [arXiv:1602.08103 \[hep-ph\]](#).
- [63] S. Schmiemann, J. Harz, B. Herrmann, M. Klasen, and K. Kovařík, *Phys. Rev. D* **99**, 095015 (2019), [arXiv:1903.10998 \[hep-ph\]](#).
- [64] J. Harz, M. Klasen, M. Y. Sassi, and L. P. Wiggering, *Phys. Rev. D* **107**, 056020 (2023), [arXiv:2210.03409 \[hep-ph\]](#).
- [65] T. Binder, M. Garny, J. Heisig, and S. Lederer, *Bsffast: Rapid computation of bound-state effects on annihilation in the early universe* (2025), [arXiv:2512.23812 \[hep-ph\]](#).
- [66] B. D. Sáez, F. Rojas-Abatte, and A. R. Zerwekh, *Phys. Rev. D* **99**, 075026 (2019), [arXiv:1810.06375 \[hep-ph\]](#).
- [67] E. W. Kolb and M. S. Turner, *The Early Universe*, Frontiers in Physics (CRC Press, Boca Raton, FL, 1994).
- [68] M. Garny, J. Heisig, B. LülF, and S. Vogl, *Phys. Rev. D* **96**, 103521 (2017), [arXiv:1705.09292 \[hep-ph\]](#).
- [69] R. T. D’Agnolo, D. Pappadopulo, and J. T. Ruderman, *Phys. Rev. Lett.* **119**, 061102 (2017), [arXiv:1705.08450 \[hep-ph\]](#).
- [70] L. J. Hall, K. Jedamzik, J. March-Russell, and S. M. West, *JHEP* **03**, 080, [arXiv:0911.1120 \[hep-ph\]](#).
- [71] L. Covi, J. E. Kim, and L. Roszkowski, *Phys. Rev. Lett.* **82**, 4180 (1999), [arXiv:hep-ph/9905212](#).
- [72] J. L. Feng, A. Rajaraman, and F. Takayama, *Phys. Rev. D* **68**, 063504 (2003), [arXiv:hep-ph/0306024](#).
- [73] M. Garny and J. Heisig, *Phys. Rev. D* **98**, 095031 (2018), [arXiv:1809.10135 \[hep-ph\]](#).
- [74] J. Harz and K. Petraki, *Phys. Rev. D* **97**, 075041 (2018), [arXiv:1711.03552 \[hep-ph\]](#).
- [75] J. Harz and K. Petraki, *JHEP* **04**, 130, [arXiv:1901.10030 \[hep-ph\]](#).
- [76] M. Garny and J. Heisig, *Phys. Rev. D* **105**, 055004 (2022), [arXiv:2112.01499 \[hep-ph\]](#).
- [77] T. Binder, M. Garny, J. Heisig, S. Lederer, and K. Urban, *Phys. Rev. D* **108**, 095030 (2023), [arXiv:2308.01336 \[hep-ph\]](#).
- [78] M. Beneke, T. Binder, L. de Ros, M. Garny, and S. Lederer, *JHEP* **02**, 189, [arXiv:2411.08737 \[hep-ph\]](#).
- [79] S. Cassel, *J. Phys. G* **37**, 105009 (2010), [arXiv:0903.5307 \[hep-ph\]](#).
- [80] S. El Hedri, A. Kaminska, and M. de Vries, *Eur. Phys. J. C* **77**, 622 (2017), [arXiv:1612.02825 \[hep-ph\]](#).
- [81] R. Iengo, *JHEP* **05**, 024, [arXiv:0902.0688 \[hep-ph\]](#).
- [82] X. Yao and B. Müller, *Physical Review D* **100**, 10.1103/physrevd.100.014008 (2019).
- [83] H. A. Bethe and E. E. Salpeter, *Quantum Mechanics of One- and Two-Electron Atoms* (Springer, New York, 1957) first edition.
- [84] S. Biondini, N. Brambilla, G. Qerimi, and A. Vairo, *JHEP* **07**, 006, [arXiv:2304.00113 \[hep-ph\]](#).
- [85] T. Binder, A. Filimonova, K. Petraki, and G. White, *Phys. Lett. B* **833**, 137323 (2022), [arXiv:2112.00042 \[hep-ph\]](#).
- [86] K. Petraki, M. Postma, and M. Wiechers, *JHEP* **06**, 128, [arXiv:1505.00109 \[hep-ph\]](#).
- [87] A. Mitridate, M. Redi, J. Smirnov, and A. Strumia, *JCAP* **05**, 006, [arXiv:1702.01141 \[hep-ph\]](#).
- [88] C. Gross, A. Mitridate, M. Redi, J. Smirnov, and A. Strumia, *Phys. Rev. D* **99**, 016024 (2019), [arXiv:1811.08418 \[hep-ph\]](#).
- [89] N. Aghanim *et al.* (Planck), *Astron. Astrophys.* **641**, A6 (2020), [Erratum: *Astron. Astrophys.* 652, C4 (2021)], [arXiv:1807.06209 \[astro-ph.CO\]](#).
- [90] S. Colucci, B. Fuks, F. Giacchino, L. Lopez Honorez, M. H. G. Tytgat, and J. Vandecasteele, *Phys. Rev. D* **98**,

- 035002 (2018), [arXiv:1804.05068 \[hep-ph\]](#).
- [91] M. Cahill-Rowley, S. El Hedri, W. Shepherd, and D. G. E. Walker, *Phys. Dark Univ.* **22**, 48 (2018), [arXiv:1501.03153 \[hep-ph\]](#).
- [92] A. Schuessler and D. Zeppenfeld, in *15th International Conference on Supersymmetry and the Unification of Fundamental Interactions (SUSY07)* (2007) pp. 236–239, [arXiv:0710.5175 \[hep-ph\]](#).
- [93] J. Heisig, A. Lessa, and L. M. D. Ramos, *Physical Review D* **110**, 10.1103/physrevd.110.015031 (2024).
- [94] S. P. Martin, *Phys. Rev. D* **77**, 075002 (2008), [arXiv:0801.0237 \[hep-ph\]](#).
- [95] J. E. Younkin and S. P. Martin, *Phys. Rev. D* **81**, 055006 (2010), [arXiv:0912.4813 \[hep-ph\]](#).
- [96] M. Aaboud *et al.* (ATLAS), *Phys. Lett. B* **775**, 105 (2017), [arXiv:1707.04147 \[hep-ex\]](#).
- [97] M. Drees and M. M. Nojiri, *Phys. Rev. D* **47**, 4226 (1993), [arXiv:hep-ph/9210272](#).
- [98] M. Drees and M. Nojiri, *Phys. Rev. D* **48**, 3483 (1993), [arXiv:hep-ph/9307208](#).
- [99] J. Hisano, K. Ishiwata, and N. Nagata, *Phys. Rev. D* **82**, 115007 (2010), [arXiv:1007.2601 \[hep-ph\]](#).
- [100] P. Gondolo and S. Scopel, *JCAP* **10**, 032, [arXiv:1307.4481 \[hep-ph\]](#).
- [101] J. Hisano, R. Nagai, and N. Nagata, *JHEP* **05**, 037, [arXiv:1502.02244 \[hep-ph\]](#).
- [102] G. Arcadi, D. Cabo-Almeida, F. Mescia, and J. Virto, *JCAP* **02**, 005, [arXiv:2309.07896 \[hep-ph\]](#).
- [103] E. Del Nobile, *The Theory of Direct Dark Matter Detection: A Guide to Computations* (Springer International Publishing, 2022).
- [104] A. Ibarra, M. Reichard, and R. Nagai, *JHEP* **01**, 086, [arXiv:2207.01014 \[hep-ph\]](#).
- [105] J. Brod, A. Gootjes-Dreesbach, M. Tamaro, and J. Zupan, *JHEP* **10**, 065, [Erratum: *JHEP* 07, 012 (2023)], [arXiv:1710.10218 \[hep-ph\]](#).
- [106] J. Aalbers *et al.* (LZ), *Phys. Rev. Lett.* **135**, 011802 (2025), [arXiv:2410.17036 \[hep-ex\]](#).
- [107] M. Becker, E. Copello, J. Harz, and M. Napetschnig, *Manual for SE+BSF4DM – A micrOMEGAs package for Sommerfeld Effect and Bound State Formation in colored Dark Sectors* (2025), [arXiv:2512.02155 \[hep-ph\]](#).
- [108] G. Alguero, G. Belanger, F. Boudjema, S. Chakraborti, A. Goudelis, S. Kraml, A. Mjallal, and A. Pukhov, *Comput. Phys. Commun.* **299**, 109133 (2024), [arXiv:2312.14894 \[hep-ph\]](#).